processes

MDPI

Article

Evaluation of Moderate Collapse Characteristics and Optimization of Drilling Fluid Density for Horizontal Wells in Deepwater Gas Fields

Chenglong Li [1], Xuanhua Zhu [1], Haowei Feng [2,*], Rui Dai [1], Haolin Song [1], Zheng Liu [1], Aopeng Zhang [1], Chen Yu [1], Yulong He [1], Xin Li [1] and Chuanliang Yan [2]

[1] CNOOC China Limited, Hainan Branch, Haikou 570100, China
[2] School of Petroleum Engineering, China University of Petroleum (East China), Qingdao 266580, China
* Correspondence: 15595401668@163.com

Abstract

Conventional drilling fluid density design based on the onset of yielding may not adequately balance wellbore stability against the available mud-weight window in deepwater sandstone–mudstone interbeds, where collapse and lost-circulation risks coexist. Using three-pressure profiles, actual mud weights, and operational records from two field wells in a South China Sea deepwater gas field, a Biot poromechanically coupled Mohr–Coulomb finite element model incorporating pore-pressure diffusion and elastoplastic deformation of the rock skeleton was developed. A numerical method was proposed to characterize the potential collapse extent by the full angular width of a continuous equivalent plastic strain (PEEQ) zone intersecting the borehole wall. The plastic responses of 22 mud-weight cases were examined for two horizontal well orientations. The near-wellbore plastic-zone extent and numerical potential collapse width generally decreased with increasing mud weight. At the same mud weight, drilling parallel to the minimum horizontal principal stress produced a smaller plastic-zone angular width than drilling parallel to the maximum horizontal principal stress. For a 30° angular-width limit, the screened mud weights were 1.130 and 1.110 g/cm^3 for drilling parallel to the maximum and minimum horizontal principal stresses, respectively; relaxing this limit to 40° yielded screened values of 1.105 and 1.080 g/cm^3. The proposed cumulative-plastic-strain-based angular criterion provides a quantitative basis for selecting well orientation and optimizing mud weight while permitting limited plastic deformation under the specified model conditions.

Keywords: South China Sea gas field; deepwater horizontal well; three-pressure profile; numerical potential collapse angular width; hydro-mechanical coupling; drilling fluid density

Check for updates

Academic Editor: Tianshou Ma

Received: 13 September 2026
Revised: 15 October 2026
Accepted: 19 October 2026
Published: 21 October 2026

Copyright: © 2026 by the authors. Licensee MDPI, Basel, Switzerland. This article is an open access article distributed under the terms and conditions of the Creative Commons Attribution (CC BY) license.

1. Introduction

Deepwater and deep hydrocarbon resources are increasingly important targets for offshore exploration and development. Increasing water depth, reservoir burial depth, and horizontal-section length complicate formation pressures, in situ stresses, and temperature–pressure conditions, raising the risks of wellbore collapse, tight holes, cavings, stuck pipes, and lost circulation. Although horizontal wells increase reservoir contact, the principal-stress configuration in the borehole cross-section changes with inclination and azimuth, while open-hole exposure times may increase considerably. Consequently, wellbore stability and mud-weight optimization are critical to safe and efficient deepwater gas development [1–3]. Transient heat exchange during deep-well circulation can also redistribute

energy near the borehole, and active cooling can substantially alter the bottomhole circulating temperature [4]. These thermal effects may modify near-wellbore stresses and the mud-weight window; they are excluded here to isolate hydro-mechanical coupling and are reserved for future thermo-hydro-mechanical (THM) modeling.

Traditional wellbore stability studies have focused on stress redistribution, rock failure criteria, and critical collapse pressure. Bradley, Aadnoy, and Chenevert established analytical approaches for inclined and highly deviated boreholes [5,6], whereas Zoback, Mastin, and Peška examined breakout orientation and its relationships with well deviation, in situ stress, and failure mode [7–9]. Laboratory work by Haimson, Lee, and colleagues identified compressive-shear, tensile, and progressive breakout mechanisms under different lithological and stress conditions [10–12]. Although these studies underpin conventional stability evaluation, the onset of local yielding does not necessarily coincide with operationally unacceptable wellbore failure. Research on block reconstruction and chain collapse in tunnels, together with two-stage cascading-failure frameworks, suggests that local failure may propagate through structural reorganization or failure of adjacent regions [13,14].

Field experience indicates that localized wellbore breakout does not invariably result in unacceptable wellbore instability. Breakout angular width has previously been used for risk classification and moderate-collapse mud-weight design [15,16]. Accordingly, neither permitting local failure nor selecting 30°/40° risk scenarios is claimed as a new concept. Instead, this study examines how near-wellbore pore pressure, stress redistribution, cumulative PEEQ, and the connected plastic-zone angular extent jointly respond to mud weight and well orientation under specified coupled hydro-mechanical boundary conditions.

Three limitations remain in existing moderate-collapse studies. First, the links among engineering angular-width criteria, pore-pressure diffusion, three-dimensional near-wellbore stress redistribution, and accumulated plastic strain are not sufficiently explicit. Second, numerical predictions are rarely interpreted jointly with three-pressure profiles, field mud weights, and caliper responses. Third, differences in the mechanical, hydraulic, and drilling-fluid response of sandstone and mudstone make a single mud-weight lower limit inappropriate for interbedded intervals. The investigated South China Sea deepwater gas field contains pronounced sandstone–mudstone interbeds, with backreaming, tight holes, cavings, and lost circulation reported in some intervals. It therefore provides an engineering setting for lithology- and orientation-specific mud-weight optimization under limited allowable failure.

Two anonymized vertical field wells, X1 and X2, were used to constrain the pressure window, actual mud weights, and operational response; usable caliper measurements were additionally available for X1. A coupled hydro-mechanical elastoplastic model was then established for representative sandstone in a planned horizontal development well. PEEQ zones, pore-pressure fields, and near-wellbore stresses were evaluated at different mud weights and well orientations, with the numerical potential collapse width used to characterize the extent of possible compressive-shear failure. Field pressure windows, inclination–azimuth trends, and numerical predictions were integrated to develop a graded mud-weight control strategy for representative sandstone.

2. Field Problem and Evidence from Reference Wells

2.1. Engineering and Geological Characteristics of the Study Area

The study area is an anonymized deepwater gas field in the South China Sea. Wells X1 and X2 are vertical field wells used to constrain the pressure window, actual mud weights, and operational response. The target intervals consist mainly of interbedded mudstone, silty mudstone, and sandstone, with local argillaceous siltstone and fine-grained sandstone, resulting in marked lithological heterogeneity. The field wells provide qualitative

evidence that conditions below a conventional fully stable mud-weight limit may remain operationally manageable. In contrast, the subsequent finite element model represents a sandstone interval in a planned 8½ in horizontal development well.

Formation pressures in the target gas field are generally near normal, although locally elevated pressure occurs. Actual mud weights were approximately 1.30–1.32 g/cm^3 in X1 and 1.21–1.25 g/cm^3 in X2. Both reference wells are vertical; their water depths are 1445.00 and 1362.05 m, respectively. The measured depths (MD) and true vertical depths (TVD) at total depth are 5188/5188 m and 4267/4267 m, respectively. The depth axes in Figures 1 and 2 therefore indicate rotary-table-referenced MD, numerically equivalent to TVD in these vertical wells. Both 12¼ in intervals were drilled with HEM water-based mud, over 3939.00–4951.76 m in X1 and 3645.00–4267.00 m in X2. Complete inclination–azimuth survey series were unavailable for continuous trajectory comparison; therefore, neither field well is used to validate the azimuthal response of a horizontal borehole. The orientation effects are investigated separately using analytical and numerical horizontal-well models. For consistent reporting, the operation-level open-hole exposure period was defined as the interval from commencement of the 12¼ in section to the start of the first wireline logging run: approximately 120.25 h in X1 and 84.25 h in X2. The first X1 logging run included caliper measurements, but it was conducted after backreaming, short trips, mud conditioning, and other hole-conditioning operations.

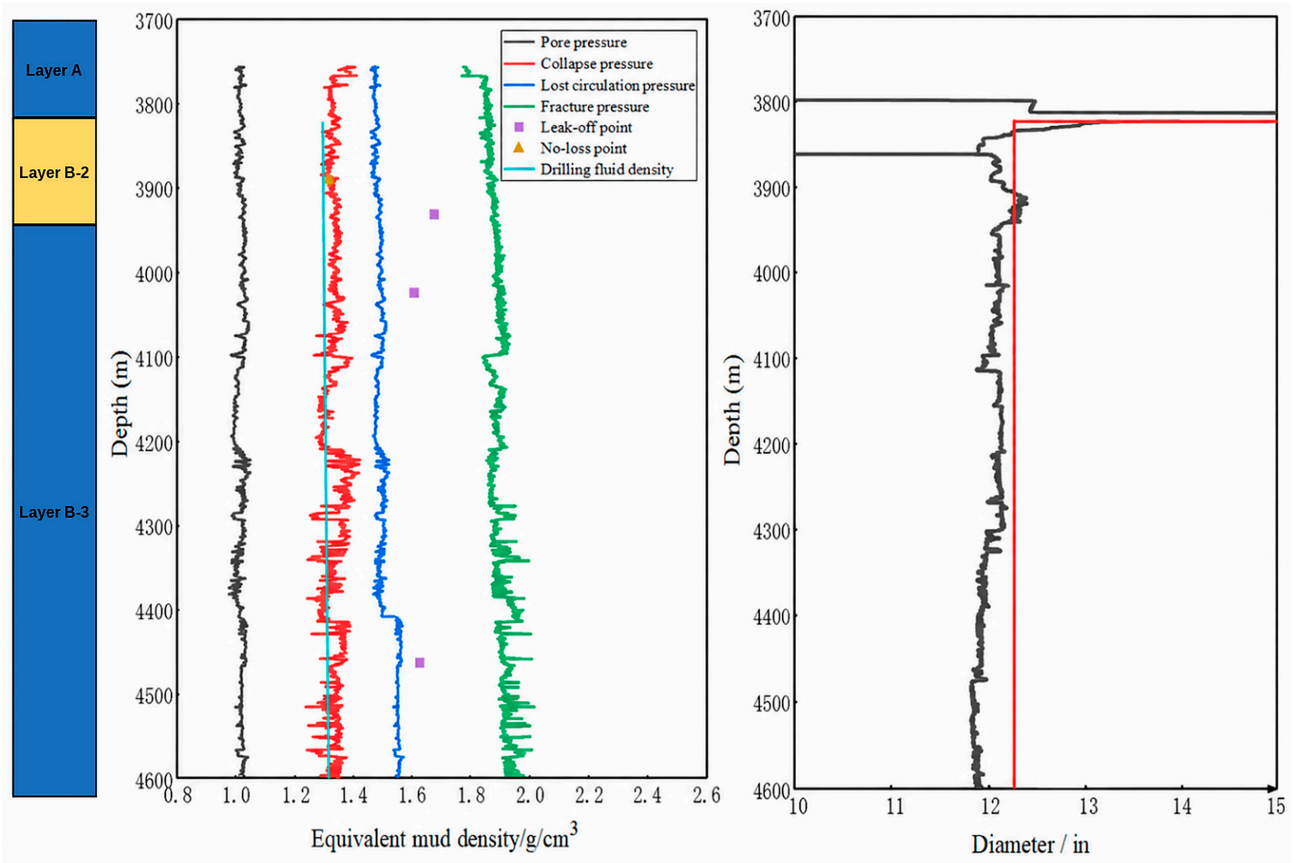


Figure 1. Three-pressure profile, actual drilling fluid density, and caliper response in Well X1. In the right panel, the black curve denotes the measured caliper diameter and the red line denotes the nominal 12¼-in borehole diameter.

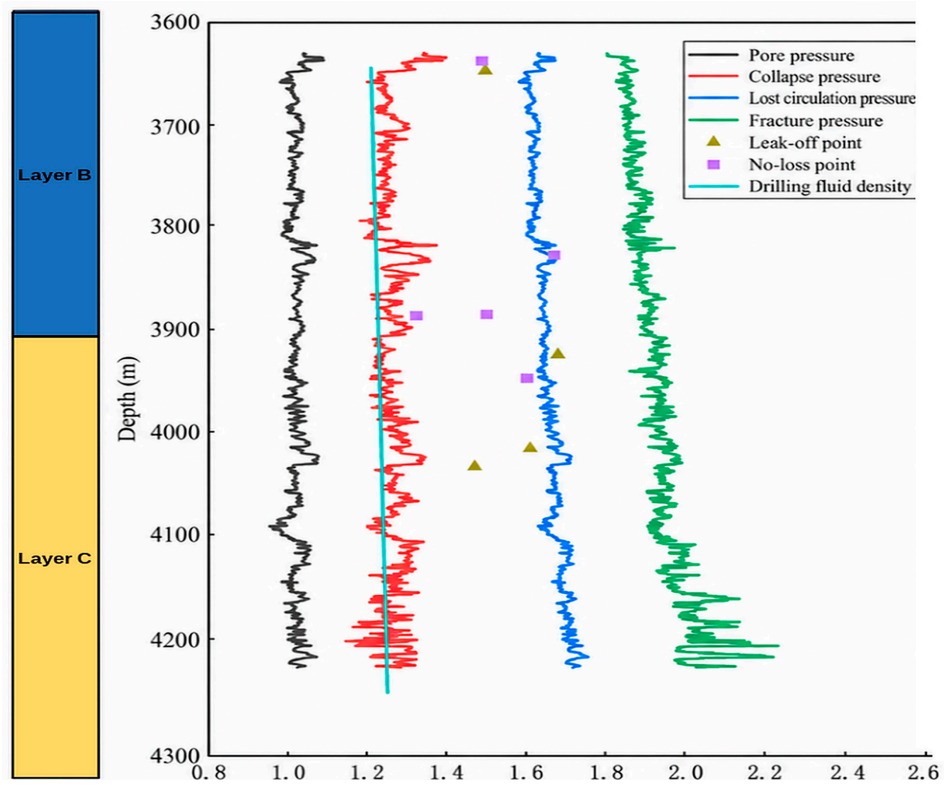


Figure 2. Three-pressure profile and actual drilling fluid density in Well X2 (conventional caliper data were unavailable in the final well report).

2.2. Three-Pressure Profiles, Actual Mud Weights, and Caliper Response

The X1 analysis interval extends from 3756.6 to 4598.2 m and covers several sandstone–mudstone interbeds. As shown in Figure 1, the pore-pressure equivalent mud weight is generally approximately 1.0 g/cm^3; the actual mud weight is approximately 1.30–1.32 g/cm^3; the lost-circulation pressure is approximately 1.50–1.65 g/cm^3; and the fracture pressure is approximately 1.80–2.00 g/cm^3. The relationship between calculated collapse pressure and actual mud weight differs by lithology and interval. In some mudstone or interbedded intervals, the collapse-pressure equivalent mud weight exceeds the actual mud weight, whereas in sandstone and relatively stable intervals, it may be close to or below that weight. Thus, only local intervals exhibiting theoretical collapse risk but an ultimately manageable caliper response are considered field evidence for moderate collapse.

The X2 analysis interval extends from 3630.0 to 4242.6 m and lies predominantly in sandstone–mudstone interbeds. Figure 2 shows a pore-pressure equivalent mud weight of approximately 1.0–1.1 g/cm^3, an actual mud weight of 1.21–1.25 g/cm^3, a lost-circulation pressure of approximately 1.60–1.75 g/cm^3, and a fracture pressure of approximately 1.80–2.20 g/cm^3. As in X1, the relationship between theoretical collapse pressure and actual mud weight varies among lithologies and intervals. The final X2 completion report contains no conventional caliper data; consequently, X2 is not used for quantitative caliper validation. Its pressure window, mud weights, lost-circulation and well-control incidents, and tripping records are used only to assess operational manageability.

Together, the two wells show that actual mud weights generally exceeded the pore-pressure lower bound while retaining some margin below the lost-circulation and fracture-pressure upper bounds. Nevertheless, theoretical collapse pressures may have exceeded actual mud weights in some mudstone or sandstone–mudstone intervals. X1 exhibited an overall manageable final borehole diameter, although its caliper was acquired after backreaming, short trips, and mud conditioning and therefore provides only evidence of

the final operational hole condition. X2 contributes pressure-window and operational-response evidence but no conventional caliper data. These observations indicate that the conventional collapse pressure is useful for delineating incipient-yield risk but is not itself a threshold for operationally unacceptable failure.

3. Computational Methodology and Coupled Hydro-Mechanical Model

3.1. Geometry and Basic Assumptions

A three-dimensional wellbore stability model was constructed using Abaqus/Standard 2024 for representative sandstone in a planned horizontal development well. The borehole radius was R = 0.108 m, consistent with an 8½ in reservoir hole (diameter 0.2159 m; radius 0.10795 m) in the engineering design. The 12¼ in open-hole interval in the reference field wells serves only as operational evidence and does not represent the same hole section as the numerical model. The outer boundary was located at least 20R from the borehole center to limit finite-domain effects. Two horizontal-well orientations were considered, with the well axis parallel to the maximum or minimum horizontal principal stress. The representative geometry and mesh are shown in Figure 3.

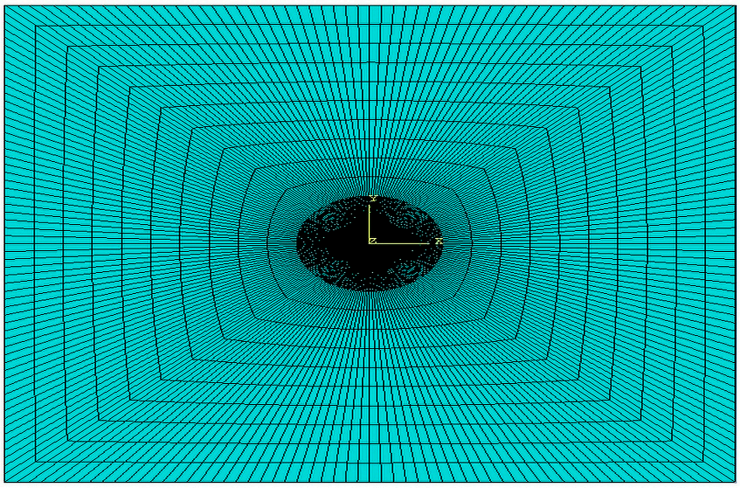


Figure 3. Geometry and mesh of the representative horizontal development-well model for the South China Sea gas field.

A formation principal-stress coordinate system, G, was defined with axes parallel to the maximum horizontal principal stress σH, minimum horizontal principal stress σh, and vertical principal stress σv. With compression taken as positive, the far-field total stress tensor is $\sigma G = \mathrm{diag}(\sigma H, \sigma h, \sigma v)$. In the numerical implementation, the borehole axis remains coincident with the Abaqus2024 global *Z*-axis; the two drilling orientations are represented by permuting the prescribed initial principal-stress components rather than rotating the borehole geometry. For a well parallel to σH, the global X-, Y-, and Z-axes correspond to σh, σv, and σH, respectively, giving $\sigma W,H = \mathrm{diag}(\sigma h, \sigma v, \sigma H)$. For a well parallel to σh, they correspond to σH, σv, and σh, giving $\sigma W,h = \mathrm{diag}(\sigma H, \sigma v, \sigma h)$. These tensors use a compression-positive convention, whereas compressive initial effective stresses in Abaqus are negative and must be distinguished from the prescribed total in situ stresses and initial pore pressure. For a general well orientation, the orthogonal direction-cosine matrix Q transforms the stress tensor as $\sigma W = Q\sigma GQ^{T}$.

For near-wellbore stress analysis, a local cylindrical coordinate system centered on the borehole axis was defined during Abaqus post-processing. Cartesian stresses were resolved into radial (σrr), circumferential or hoop (σθθ), and axial (σzz) components. When the local cylinder axis coincides with global +Z and the 0° reference direction is global +X,

θ is measured counterclockwise from +X toward +Y according to the right-hand rule about +Z. Thus, θ = 0° lies on the σh principal-stress axis for drilling parallel to σH and on the σH axis for drilling parallel to σh; θ = 90° lies on the vertical principal-stress axis in both cases. This convention is used for all near-wellbore angles and potential collapse widths.

To isolate mud-weight and well-orientation effects in representative sandstone, the following assumptions were adopted: (1) the sandstone is a homogeneous, isotropic, saturated porous medium; (2) its elastoplastic response obeys the small-strain assumption; (3) single-phase pore-fluid flow follows Darcy's law; (4) instability is identified principally through compressive-shear plastic yielding, without explicit simulation of block detachment, transport, or large-deformation updating of borehole geometry; and (5) temperature effects, bedding anisotropy, natural fractures, and drilling-fluid–formation chemical interactions are neglected. Therefore, the finite element results in Sections 3–5 apply only to the representative sandstone under the stated stress, pore-pressure, mechanical, hydraulic, and borehole conditions and must not be extrapolated directly to mudstone or an entire interbedded interval. Earlier studies of drilling-fluid–shale interactions demonstrated that chemical potential, solute diffusion, and thermal–pressure coupling can affect stability [17–20], and subsequent work examined poroelastic–thermal–chemical mechanisms [21–23]. These effects are acknowledged as exclusions rather than mechanisms represented by the present sandstone model.

3.2. Hydro-Mechanical Coupling Formulation

The formation surrounding a deepwater horizontal well may be represented as a saturated porous medium consisting of a solid skeleton and pore fluid. Drilling fluid pressure applied at the borehole wall changes the stresses carried by the skeleton, while pore-pressure diffusion modifies the effective stresses in the near-wellbore region. A coupled description of solid deformation and pore-fluid flow is therefore required. Biot's poroelasticity theory is used to formulate the governing hydro-mechanical equations [24–27].

3.2.1. Governing Equations for the Solid Skeleton

The solid skeleton satisfies the static equilibrium equation:

$$\nabla \cdot \sigma + \mathbf{b} = 0 \tag{1}$$

where σ is the total stress tensor, and b denotes the body-force vector. In wellbore stability analysis, σ is primarily determined by the in situ stress field, drilling-fluid pressure at the borehole wall, and pore pressure. $\sigma b \sigma$.

The strain–displacement relation is:

$$\varepsilon = \frac{1}{2}\left[\nabla \mathbf{u} + (\nabla \mathbf{u})^T\right] \tag{2}$$

where ε denotes the strain tensor, and u is the displacement vector. $\boldsymbol{\varepsilon u}$.

Deformation and yielding of the rock skeleton in a porous medium are governed primarily by effective stress. In the continuum equations, tensile stresses and strains are taken as positive. The effective stress tensor is expressed as:

$$\boldsymbol{\sigma'} = \boldsymbol{\sigma} + \alpha p \mathbf{I} \tag{3}$$

where σ′ and σ are the effective and total stress tensors, respectively, p denotes pore pressure, α is Biot's effective stress coefficient, and I is the identity tensor. Here, α = 1.

The isotropic linear-elastic constitutive relationship is:

$$\boldsymbol{\sigma}' = \mathbf{D}^e : (\boldsymbol{\varepsilon} - \boldsymbol{\varepsilon}^p) \tag{4}$$

where D^e is the elastic stiffness matrix, ε is the total strain tensor, and ε^p is the plastic strain tensor. Before yielding, $\varepsilon^p = 0$; plastic strains accumulate once the near-wellbore effective stress state reaches the yield surface.

The Mohr–Coulomb criterion was adopted to describe shear yielding around the borehole. Its cohesion and friction-angle parameters have direct physical interpretations and can be related to laboratory measurements. Comparative studies of three-dimensional rock failure criteria suggest that the Mohr–Coulomb model provides a conservative approximation of compressive-shear plastic zones but does not account for the intermediate principal stress [28–33]. With compression taken as positive, the Mohr–Coulomb yield function is:

$$F = (\sigma_1' - \sigma_3') - (\sigma_1' + \sigma_3') \sin\varphi - 2c\cos\varphi \tag{5}$$

Here, σ'_1 and σ'_3 are the major and minor effective principal stresses, c is cohesion, and φ is the internal friction angle. $F < 0$ denotes an elastic trial stress state and $F = 0$ the yield condition; subsequent loading produces irreversible plastic strain. Equivalent plastic strain (PEEQ) was used to quantify accumulated plastic deformation, and the continuous PEEQ zone connected to the borehole wall was taken as the potential collapse region.

3.2.2. Governing Equations for Pore-Fluid Flow

Under saturated single-phase flow, pore-fluid motion follows Darcy's law. Equation (6) uses the intrinsic permeability tensor k (m^2), whereas the numerical model specifies the saturated hydraulic conductivity tensor K (m/s). These quantities are related by $K = (\gamma w/\mu)k$, where γw is the fluid unit weight, and μ is the dynamic viscosity. The homogeneous and isotropic representative sandstone is assigned $K = khI$, with $kh = 1.0 \times 10^{-8}$ m/s and zero off-diagonal components; I is the identity tensor. The pore-fluid unit weight is 9.8×10^3 N/m^3, and the initial void ratio $e_0 = 0.08$ corresponds to a porosity $n_0 = e_0/(1 + e_0) = 0.0741$ (7.41%). The Biot effective stress coefficient is $\alpha = 1$. These are prescribed model parameters describing the hydraulic behavior and initial pore structure of the representative sandstone.

$$\mathbf{q} = -\frac{\mathbf{k}}{\mu}(\nabla p - \rho_f \mathbf{g}) \tag{6}$$

Here, q is the pore-fluid seepage flux, k denotes intrinsic permeability, μ is the dynamic viscosity, ρf is the pore-fluid density, and g is gravitational acceleration. If gravity is neglected or comparatively weak, the equation simplifies to: $qk\mu\rho_f g$

$$\mathbf{q} = -\frac{\mathbf{k}}{\mu}\nabla p \tag{7}$$

Pore-fluid mass conservation can be written as:

$$\frac{\partial \zeta}{\partial t} + \nabla \cdot \mathbf{q} = Q \tag{8}$$

where ζ is the change in fluid content per unit bulk volume, Q is the fluid source/sink term, and t denotes time. In a saturated porous medium, the fluid-content increment depends on skeleton volumetric strain and pore-pressure change: ζQt

$$\zeta = \alpha\varepsilon_v + \frac{p}{M} \tag{9}$$

$$\alpha \frac{\partial \varepsilon_v}{\partial t} + \frac{1}{M}\frac{\partial p}{\partial t} - \nabla \cdot \left(\frac{\mathbf{k}}{\mu}\nabla p\right) = Q \quad (10)$$

Equation (10) shows that pore-pressure evolution is governed not only by permeability, fluid viscosity, and the pressure gradient but also by deformation of the rock skeleton. Near-wellbore compaction or dilation changes pore volume and consequently modifies pore pressure and the effective stress state.

3.2.3. Hydro-Mechanical Coupling Mechanisms

The hydro-mechanical response involves two principal mechanisms.

First, pore pressure modifies the stresses transmitted through the rock skeleton according to the effective stress principle. As Equation (3) shows, pore-pressure changes at a fixed total stress alter the effective stress and hence the Mohr–Coulomb yield response. Increasing mud weight in a horizontal borehole simultaneously raises radial support pressure and changes the near-wellbore pore-pressure boundary. Accordingly, stability depends on the combined effects of drilling-fluid pressure, in situ stress, pore pressure, and rock strength.

Second, skeleton deformation changes the pore volume and influences pore-pressure diffusion. Under the combined action of in situ stress and drilling-fluid pressure, volumetric strain εv modifies pore-fluid storage space and subsequent pressure evolution. Once a plastic zone develops, local volumetric deformation and stress redistribution can further modify pore-pressure gradients and reorganize near-wellbore effective stresses.

3.3. Rock Mechanical Properties

Elastic and strength properties of the representative sandstone were selected using laboratory rock-mechanics tests, well-log interpretation, and formation data for the target area (Table 1). Uniaxial compressive strengths in the overlying sandstone–mudstone intervals are mainly 20–60 MPa, while values in the target formation vary more widely, approximately 40–100 MPa, because of interbedding and contrasts in rock stiffness and strength. To isolate the effects of mud weight and well orientation, constant elastic, strength, and hydraulic properties were assigned to the representative sandstone. Cohesion c and friction angle φ are the primary Mohr–Coulomb strength inputs; uniaxial compressive strength (UCS) is used for parameter-consistency checking.

Table 1. Mechanical and hydraulic properties of the representative sandstone in the South China Sea gas field.

Parameter	Symbol	Value
Young's modulus	E	12 201.6 MPa
Poisson's ratio	ν	0.22
Bulk density	ρ	2.50 g/cm^3
Cohesion	c	8.05 MPa
Internal friction angle	φ	50.3°
Uniaxial compressive strength	UCS	45.0 MPa
Initial void ratio	e_0	0.08
Initial porosity	n_0	0.0741 (7.41%)
Isotropic hydraulic conductivity	Kh	1.0×10^{-8} m/s
Pore-fluid unit weight	γw	9800 N/m^3
Biot effective stress coefficient	α	1.0

3.4. In Situ Stresses and Boundary Conditions

The initial formation pore pressure was 41.78 MPa (Table 2), and the far-field pore-pressure boundary was held constant during transient analysis. Drilling-fluid support pressure and a prescribed pore pressure were simultaneously imposed at the borehole wall,

with the latter set equal to the mud pressure, p(R,t) = Pw, to represent full hydraulic communication between borehole fluid and the formation pore network. Both the mechanical wall pressure and prescribed wall pore pressure were varied with mud weight; for mud weights of 1.12 and 1.18 g/cm^3, both pressures were 45.692 and 48.140 MPa, respectively. This condition neglects mud cake sealing and additional flow resistance at the borehole wall. It is an idealized fully communicating hydraulic end member, used to investigate coupled pore-pressure diffusion, effective-stress redistribution, and plastic deformation driven by drilling-fluid pressure.

Table 2. In situ stresses and borehole-pressure parameters for the representative interval.

Parameter	Symbol	Value
Maximum horizontal principal stress	σH	69.74 MPa
Minimum horizontal principal stress	σh	63.77 MPa
Vertical principal stress	σv	78.16 MPa
Pore pressure	Pp	41.78 MPa
Representative calculation depth (TVD)	H	4158.7 m
Drilling fluid density	ρm	1.05–1.19 g/cm^3

According to Biot's effective stress principle, with compression taken as positive, radial effective stress is $\sigma'r = \sigma r - \alpha p$. When the mechanical borehole-wall pressure and pore pressure both equal Pw and $\alpha = 1$, the ideal wall boundary satisfies $\sigma'r(R) = 0$. This expresses the mechanical consistency of the prescribed normal traction and pore pressure under the fully communicating boundary assumption.

The hydrostatic drilling-fluid pressure is calculated as:

$$P_w = 0.00981\rho_m H \quad (11)$$

where Pw is the hydrostatic borehole pressure (MPa), ρm is drilling-fluid density (g/cm^3), and H is the representative true vertical depth (TVD, m).

3.5. Numerical Implementation, Mesh, and Simulation Cases

Eight-node coupled pore-pressure/displacement hexahedral elements (C3D8P) were used to solve the three displacement components and pore-pressure degree of freedom. Two analysis stages were conducted. A Geostatic step first established equilibrium between in situ stresses and pore pressure, followed by a transient Soils pore-pressure/displacement analysis step in Abaqus/Standard to simulate stress redistribution and pressure diffusion induced by borehole pressure. The model thus uses transient rather than steady-state flow. The total physical time of Step2 was 2.592×10^6 s (30 days). Automatic time stepping was used, with an initial increment of 1 s, a minimum increment of 1.0×10^{-10} s, a maximum increment of 1.0×10^4 s, a maximum of 100,000 increments, and a maximum allowable pore-pressure change of 1.0×10^8 Pa per increment.

A structured circumferential mesh was locally refined near the borehole, with element size increasing away from the wall (Figure 4). During post-processing, a circular path centered on the borehole was defined on the undeformed geometry at the mid-axial plane. The variables S11, S22, S33, S12, POR, and PEEQ were extracted in the local cylindrical coordinate system. Nine baseline mud weights were simulated for each of the σH- and σh-parallel well orientations; four refined cases were then added at 1.105 and 1.130 g/cm^3 along σH and 1.080 and 1.105 g/cm^3 along σh, for 22 PEEQ datasets in total. Table 3 lists mud-weight/pressure conversions. The orientation-specific PEEQ angular-width results are discussed in Section 4.5.3. Circumferential angular width was determined using uniform 1.5° path sampling.

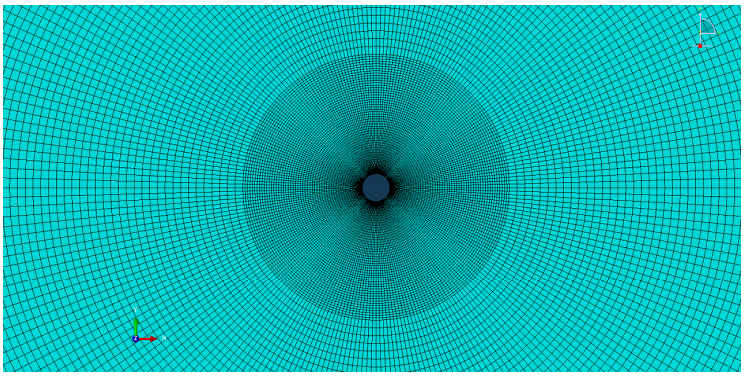


Figure 4. Locally refined mesh near the borehole wall. The central circular opening represents the borehole.

Table 3. Drilling-fluid density and hydrostatic borehole-pressure conversions at the representative depth, including locally refined mud-weight cases.

Case	Mud Weight (g/cm^3)	Borehole Pressure (MPa)
Case 1	1.05	42.84
Case 2	1.07	43.65
Case 3	1.08	44.06
Case 4	1.09	44.47
Case 5	1.10	44.88
Case 6	1.11	45.29
Case 7	1.12	45.69
Case 8	1.13	46.10
Case 9	1.14	46.51
Case 10	1.15	46.92
Case 11	1.16	47.32
Case 12	1.17	47.73
Case 13	1.18	48.14
Case 14	1.19	48.55
Locally refined case	1.105	45.08

3.6. Elastic Kirsch Benchmark and Simplified Onset-of-Yielding Reference

To assess whether the finite element model reproduces elastic stress redistribution around a circular borehole, a separate linear-elastic case was established for the representative horizontal well orientation without Mohr–Coulomb plasticity or pore-pressure degrees of freedom. With the well axis parallel to the maximum horizontal principal stress σH, local x, y, and z coincide with the σh, σv, and σH principal-stress axes, respectively. Using a compression-positive convention, the far-field stresses are σx = σh = 63.77 MPa, σy = σv = 78.16 MPa, and σz = σH = 69.74 MPa; Poisson's ratio is ν = 0.224437; and the uniform borehole pressure is Pw = 45.70 MPa. The circumferential angle θ is measured from local +x according to the right-hand rule about the well axis. At r = R, the classical infinite-medium Kirsch solution gives:

$$\sigma r(R,\theta) = Pw$$

$$\sigma\theta(R,\theta) = \sigma h + \sigma v - 2(\sigma h - \sigma v)\cos(2\theta) - Pw$$

$$\sigma z(R,\theta) = \sigma H - 2\nu(\sigma h - \sigma v)\cos(2\theta)$$

Radial, hoop, and axial stresses were extracted in cylindrical coordinates at 1.5° increments along the mid-borehole circumference in the independently completed linear-elastic Geostatic simulation. Figure 5 compares these predictions with the Kirsch solution around

the full circumference. The finite element and analytical results show broadly consistent peak/trough orientations and periodic variations, particularly for hoop and axial stresses. The root-mean-square errors (RMSEs) for radial, hoop, and axial stress are 2.617, 2.425, and 2.054 MPa, respectively. The comparison supports the model's ability to reproduce the principal orientations and trends of near-wellbore elastic stress concentrations.

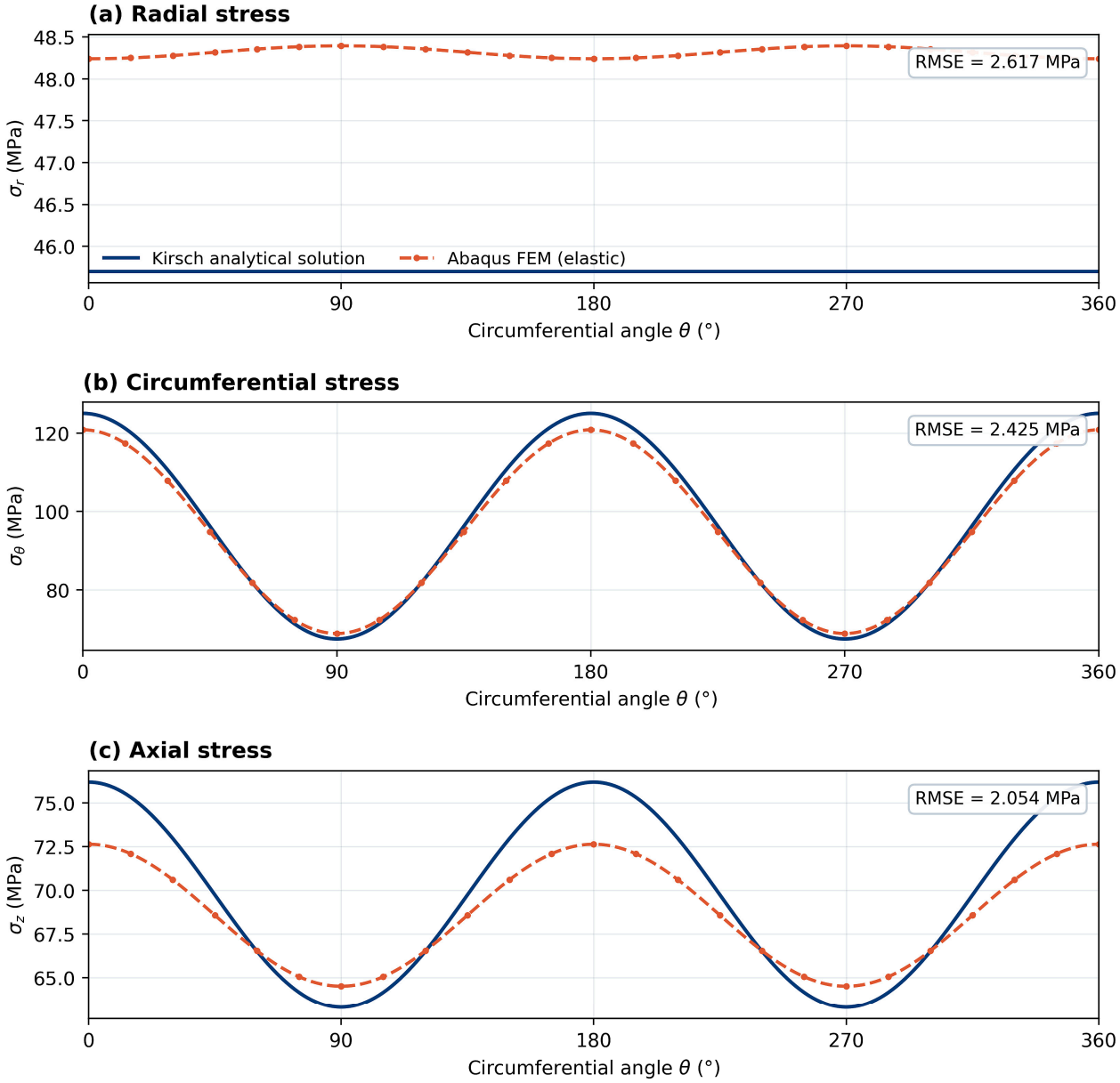


Figure 5. Comparison of the elastic Kirsch solution and Abaqus finite element results along the borehole circumference: (**a**) radial stress; (**b**) hoop stress; and (**c**) axial stress.

An analytical onset-of-yielding reference was established by combining the classical Kirsch elastic stress solution with the Mohr–Coulomb strength criterion. Assuming spatially uniform initial pore pressure $p = p_0$, the near-wellbore elastic stress distribution was evaluated for different borehole pressures. Biot's effective stress principle was then used to obtain the effective stress state. Under a compression-positive convention, the maximum and minimum effective principal stresses, σ'_1 and σ'_3, were substituted into the Mohr–Coulomb yield function:

$$F(\theta, P_w) = \sigma'_1 - N_\varphi \sigma'_3 - C_\varphi$$

The strength coefficients Nφ and Cφ are defined by:

$$N_\varphi = \frac{1 + sin\varphi}{1 - sin\varphi}$$

$$C_\varphi = \frac{2c\ cos\varphi}{1 - sin\varphi}$$

Here, c is cohesion, φ is the internal friction angle, θ is the circumferential angle, and Pw is the borehole pressure. When F(θ,Pw) = 0, the elastic trial stress reaches the yield surface; F(θ,Pw) ≥ 0 indicates that the trial stress meets or exceeds the Mohr–Coulomb strength envelope. The critical onset-of-yielding pressure Pc is defined as the pressure at which the most unfavorable circumferential location first reaches yield as the borehole support pressure is reduced from a stable state. Accordingly, Pc satisfies:

$$max_\theta\ F(\theta, P_c) = 0$$

Using Tables 1 and 2, with c = 8.05 MPa, φ = 50.3°, σh = 63.77 MPa, σv = 78.16 MPa, and uniform initial pore pressure p_0 = 41.78 MPa, the strength coefficients are Nφ = 7.673 and Cφ = 44.597 MPa. Over the investigated borehole-pressure range, the critical locations in the Kirsch–Mohr–Coulomb analytical reference are θ = 0° and 180°. Substitution of the effective principal stresses into F = 0 gives an onset-of-yielding pressure Pc = 46.686 MPa, equivalent to a mud weight of 1.144 g/cm^3 at the representative TVD of 4158.7 m.

As shown in Table 4, the maximum circumferential analytical yield-function value decreases from +8.62 to −16.15 MPa as the borehole pressure rises from 45.692 to 48.548 MPa, crossing zero between mud weights of 1.14 and 1.15 g/cm^3. In contrast, the single-lobe PEEQ angular width in the 30-day coupled finite element simulations decreases from 33–36° to no detectable plastic lobe at 1.19 g/cm^3. These two calculations do not represent identical internal hydraulic or constitutive states: the analytical reference assumes uniform pore pressure p_0, whereas the FEM prescribes p(R,t) = Pw at the wall and accounts for transient diffusion and accumulated plastic deformation. Their outputs thus represent the onset of yielding in an idealized elastic trial stress field and the accumulated plastic extent after a specified loading history, respectively. The difference in the corresponding mud weights should not be interpreted as a direct prediction error or as the actual pressure for rock detachment.

Table 4. Comparison of the analytical onset-of-yielding criterion at uniform initial pore pressure and the 30-day coupled FEM PEEQ angular width for a well parallel to σH.

Mud Weight (g/cm^3)	Wall Pressure (MPa)	maxθ F (MPa)	30-Day PEEQ Single-Lobe Width (°)
1.12	45.692	+8.62	33–36
1.14	46.508	+1.54	24–27
1.15	46.916	−2.00	18–21
1.18	48.140	−12.61	6–9
1.19	48.548	−16.15	0 (numerical zero)

4. Numerical Results and Engineering Optimization

4.1. Effects of Well Inclination and Azimuth on Collapse and Fracture Pressures in Sandstone and Mudstone

For the representative X1 interval, the collapse-pressure equivalent mud weight in vertical mudstone is approximately 1.20 g/cm^3, increasing generally with inclination to 1.27–1.30 g/cm^3 for horizontal wells. For sandstone, the corresponding values are

approximately 1.09 g/cm^3 in a vertical well and 1.16–1.19 g/cm^3 in a horizontal well. Thus, sandstone collapse-pressure equivalent mud weights are approximately 0.08–0.11 g/cm^3 lower than those of mudstone under comparable inclinations and azimuths, providing a lithological basis for considering a lower mud weight in sandstone intervals.

In the inclination–azimuth calculations, drilling toward the minimum horizontal principal-stress direction gives the lowest collapse pressure and highest fracture pressure, providing the widest safe mud-weight window. Conversely, drilling toward the maximum horizontal principal-stress direction yields the highest collapse pressure and lowest fracture pressure and is therefore unfavorable for both collapse and lost-circulation control. The fracture-pressure equivalent mud weight in vertical mudstone is approximately 2.00 g/cm^3, compared with an azimuth-dependent range of approximately 1.87–2.14 g/cm^3 for horizontal wells. The corresponding sandstone values are approximately 1.92 g/cm^3 and 1.87–2.20 g/cm^3, respectively. Orientation optimization can therefore lower the collapse-pressure bound and increase the fracture-pressure limit, thereby widening the safe mud-weight window (Figure 6).

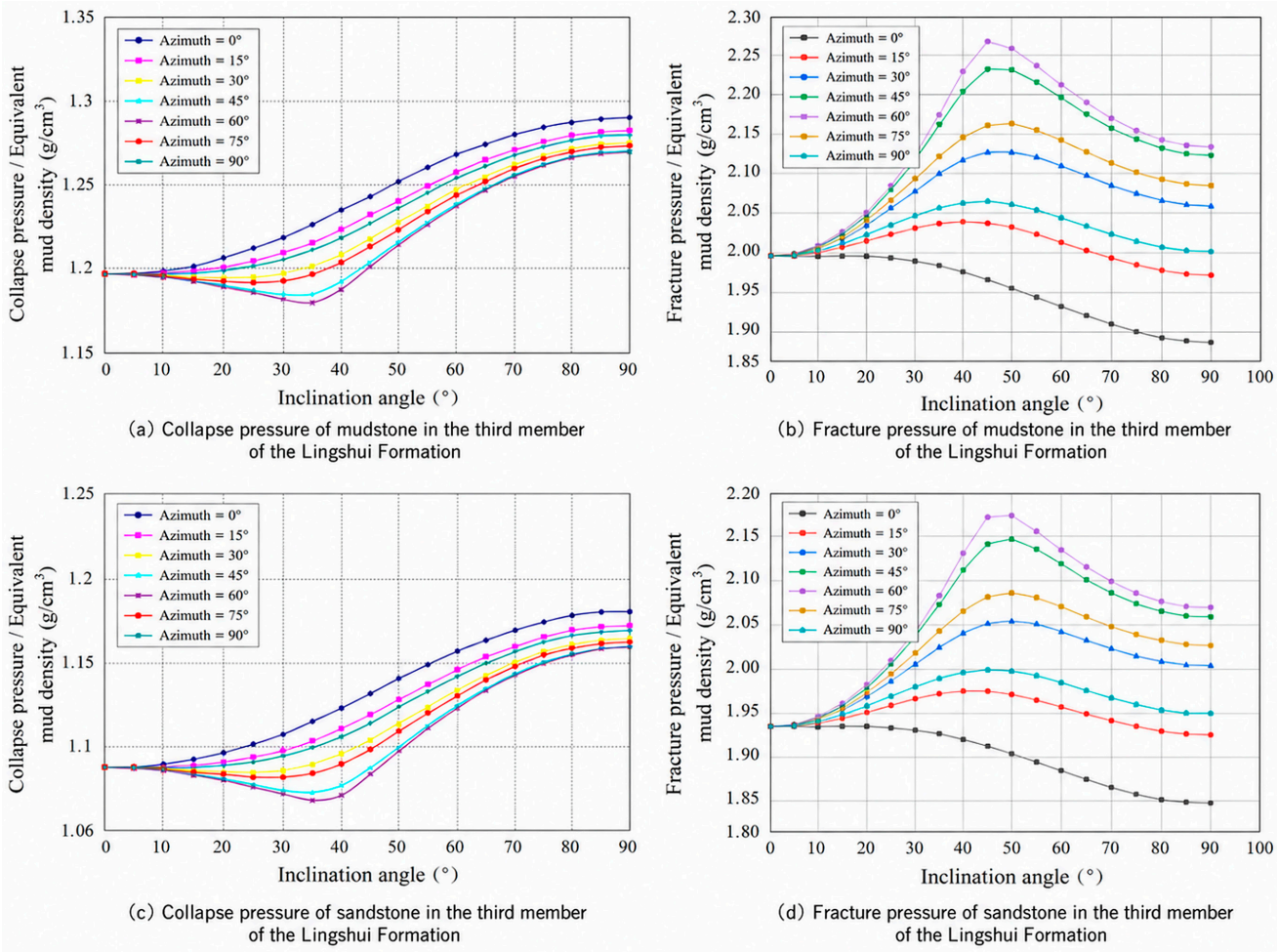


Figure 6. Variations in the collapse and fracture pressure of target mudstone and sandstone with inclination and well azimuth.

The inclination–azimuth results illustrate lithology- and orientation-dependent pressure windows. More conservative stability control is required in mudstone, whereas sandstone may provide scope for reducing mud weight below the fully stable lower bound. The mudstone and sandstone pressure curves in this section were obtained from conven-

tional wellbore stability calculations; the subsequent coupled finite element simulations represent sandstone only, and their PEEQ outcomes are not extrapolated to mudstone.

4.2. Identification of PEEQ Plastic Zones and Implications for Progressive Failure

Equivalent plastic strain (PEEQ) characterizes accumulated irreversible deformation after material yielding, and its contours can be used to identify the location and extent of near-wellbore plastic zones. Previous elastoplastic, continuum-damage, and discrete-element investigations indicate that wellbore breakout can involve local yielding, progressive damage, and subsequent growth of the affected geometry [34–37]. Initial localized damage may induce further structural changes [13,14]. Here, only a continuous PEEQ zone connected to the borehole wall is interpreted as a potential compressive-shear failure region; PEEQ > 0 does not, by itself, establish that rock fragments have detached.

4.3. Definition of Numerical Potential Collapse Angular Width and Its Relationship to Actual Breakout Width

To characterize the circumferential distribution of plastic deformation, adjacent sampling locations where PEEQ exceeds the numerical threshold of 10^{-8} are grouped into a continuous plastic lobe. The full central angle subtended by the two boundaries of one such lobe is defined as the numerical potential collapse angular width, β. If the boundary angles are θ_1 and θ_2, then:

$$\beta = \theta_2 - \theta_1 \tag{12}$$

Here, θ_1 and θ_2 denote the two boundaries of the same continuous plastic lobe. When the lobe crosses the 0° direction, the angles are unwrapped periodically before calculating their difference. β denotes the complete angular width of one lobe, not the half-angle between its centerline and either boundary. When multiple lobes occur, their widths are determined separately, and the larger value is selected for conservative assessment rather than summing the widths on opposite sides of the borehole.

Importantly, PEEQ angular width describes the spatial extent of potential plastic deformation and is not equivalent to the angular width of rock actually spalled from the borehole. Although both quantities can be expressed as central angles, an inequality for the actual breakout width βb follows only under the assumption that the detached-rock region lies entirely within the corresponding numerically identified plastic lobe:

$$\beta_b \leq \beta \tag{13}$$

Consequently, using an allowable engineering breakout width as the limit for numerical plastic angular width is a conservative assessment only under this geometric-inclusion assumption; it does not constitute a calibrated one-to-one mapping. Circumferential sampling at 1.5° also limits the resolution with which plastic-zone boundaries can be identified, so angular widths are reported as resolution-bounded intervals. The geometric definitions are illustrated in Figure 7.

4.4. Moderate-Collapse Criterion and Principles of Mud-Weight Optimization

Building on previous engineering assessments based on borehole breakout angular width [15,16], two angular limits, 30° and 40°, were selected to represent different levels of tolerated risk. The evaluation indicator is the full angular width β of a single continuous plastic lobe, as defined above. $\beta \leq 30°$ represents a more stringent limited-plasticity control scenario; $30° < \beta \leq 40°$ represents a marginally controllable scenario; and $\beta > 40°$ indicates a more extensive potential plastic region for which mud weight or well orientation should be reconsidered in conjunction with the formation pressure window and operating conditions. These limits adapt the established engineering concept of breakout-width-

based control to relative numerical plastic-zone risk, rather than constituting universal, field-calibrated thresholds.

To avoid selecting mud-weight limits from contour plots alone, a combined assessment was developed using field pressure windows and caliper responses, inclination–azimuth trends, FEM PEEQ angular domains, and engineering risk classification. Three-pressure profiles constrain the pore-pressure lower bound and the lost-circulation/fracture-pressure upper bounds. Inclination–azimuth analyses identify favorable and unfavorable orientations. FEM results quantify potential plastic-zone extent in representative sandstone at mud weights below the fully stable pressure. Caliper measurements, returned cavings, back-reaming, tight-hole incidents, and lost circulation are used only to assess overall operational manageability; they do not provide a direct calibration of actual breakout angular width.

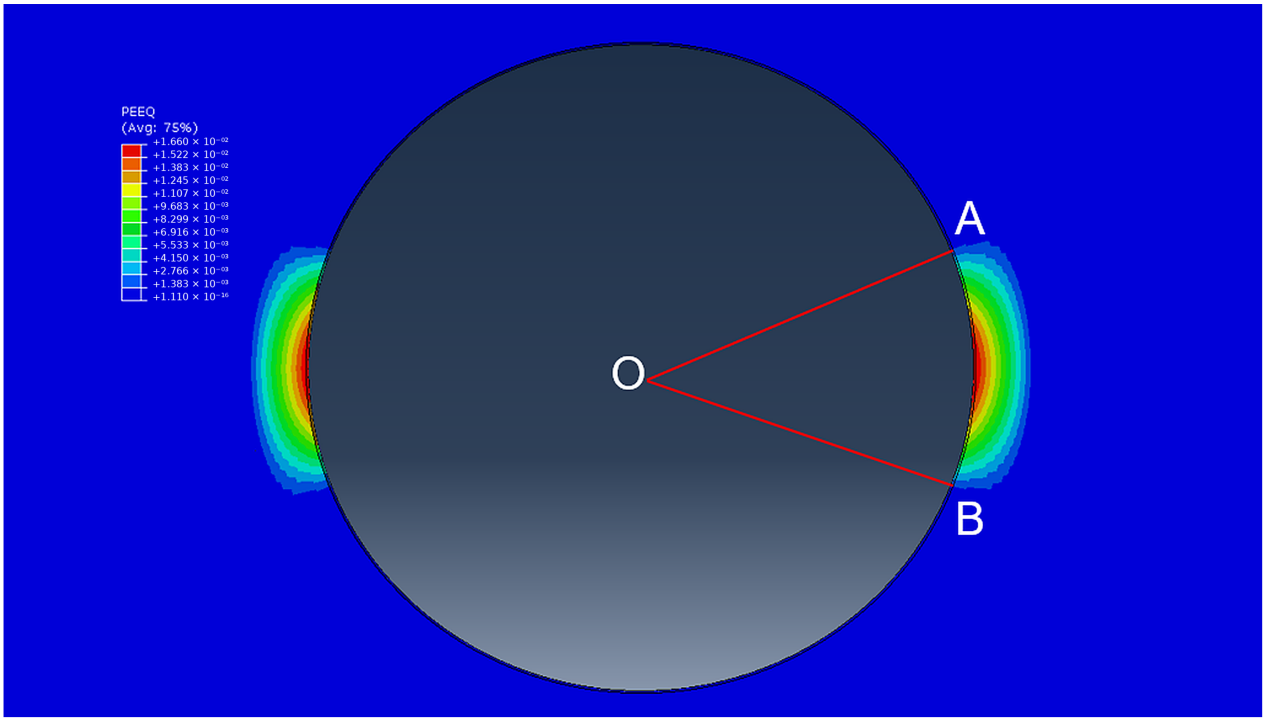


Figure 7. Geometric relationship among the PEEQ plastic angular domain, numerical potential collapse width, and actual borehole breakout width. O is the borehole center, and A and B define the angular boundaries of the connected PEEQ zone at the borehole wall; the colored bands indicate PEEQ magnitude, while the dark circular region indicates the borehole opening. The PEEQ scale is dimensionless, with blue denoting lower values and red denoting higher values.

4.5. Plastic-Zone and Potential-Collapse Angular-Width Evolution with Well Orientation

4.5.1. Drilling Parallel to the Maximum Horizontal Principal Stress

Figure 8 shows PEEQ zones at different mud weights for a well parallel to σH. The full angular width of one continuous lobe identified by the uniform path criterion is 45–48°, 39–42°, and 33–36° at 1.08, 1.10, and 1.12 g/cm^3, respectively. At 1.14, 1.15, 1.16, 1.17, and 1.18 g/cm^3, the corresponding widths are 24–27°, 18–21°, 15–18°, 12–15°, and 6–9°. At 1.19 g/cm^3, the maximum PEEQ is approximately 2.22×10^{-16}, effectively numerical zero, and no plastic lobe is detected. In contrast to previous visually estimated widths, these values are bounded by the angular resolution of discrete path sampling. Two locally refined mud-weight cases, 1.105 and 1.130 g/cm^3, yield 36–39° and 27–30°, respectively, thereby providing closer discrete constraints for the 40° and 30° risk scenarios.

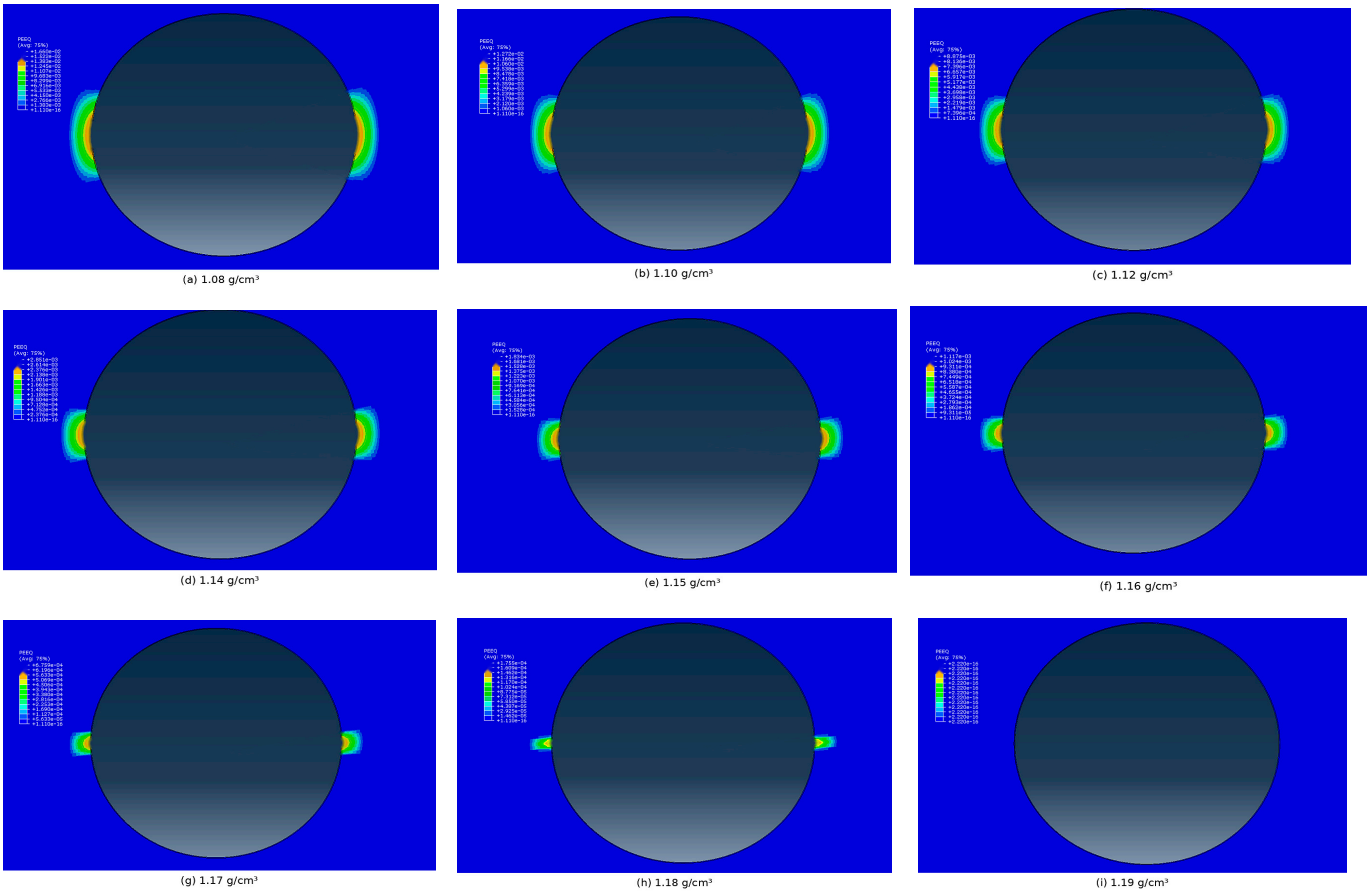


Figure 8. PEEQ plastic zones and numerical potential collapse angular widths for drilling parallel to σH: (**a**) 1.08; (**b**) 1.10; (**c**) 1.12; (**d**) 1.14; (**e**) 1.15; (**f**) 1.16; (**g**) 1.17; (**h**) 1.18; and (**i**) 1.19 g/cm^3. The dark circular region denotes the borehole opening; the surrounding colors indicate equivalent plastic strain (PEEQ) according to the legend and do not by themselves represent detached rock. Warmer colors indicate higher PEEQ values.

4.5.2. Drilling Parallel to the Minimum Horizontal Principal Stress

Figure 9 presents PEEQ zones for drilling parallel to σh. Under the same identification procedure, the single-lobe angular widths at 1.05, 1.07, 1.09, 1.10, 1.11, and 1.12 g/cm^3 are 45–48°, 39–42°, 33–36°, 30–33°, 27–30°, and 24–27°, respectively. The widths at 1.14 and 1.15 g/cm^3 are 15–18° and 9–12°. At 1.16 g/cm^3, the maximum PEEQ is approximately 2.22×10^{-16}, and no plastic lobe can be identified. Two refined cases at 1.080 and 1.105 g/cm^3 produce widths of 36–39° and 30–33°, respectively. Accordingly, the earlier visual estimates of 39.8° at 1.05 g/cm^3 and 29° at 1.10 g/cm^3 are no longer used as quantitative criteria.

4.5.3. Comparison of the Two Drilling Orientations

For the common mud-weight cases, the potential plastic angular width is consistently larger when drilling parallel to σH than when drilling parallel to σh. At mud weights of 1.10, 1.12, 1.14, and 1.15 g/cm^3, the corresponding widths are 39–42°, 33–36°, 24–27°, and 18–21° for the σH-parallel well, compared with 30–33°, 24–27°, 15–18°, and 9–12° for the σh-parallel well. The principal-stress contrast in the borehole cross-section is σv − σh = 14.39 MPa for a well parallel to σH, but σv − σH = 8.42 MPa for a well parallel to σh. The larger transverse stress contrast is consistent with the broader PEEQ lobes in the first orientation. The corresponding casewise angular-width intervals are listed in Table 5 and compared in Figure 10.

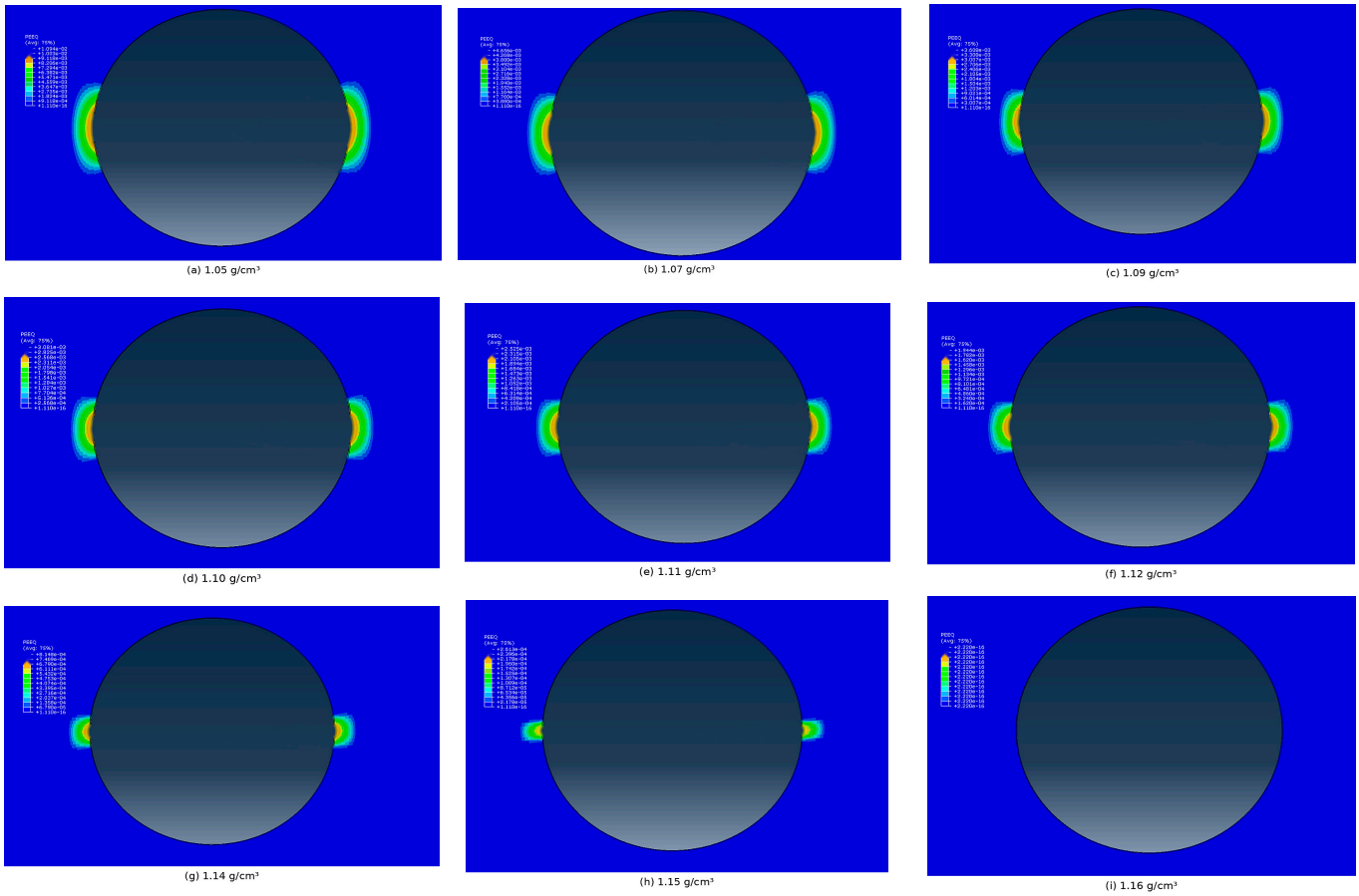


Figure 9. PEEQ plastic zones and numerical potential collapse angular widths for drilling parallel to σh: (**a**) 1.05; (**b**) 1.07; (**c**) 1.09; (**d**) 1.10; (**e**) 1.11; (**f**) 1.12; (**g**) 1.14; (**h**) 1.15; and (**i**) 1.16 g/cm^3. The dark circular region denotes the borehole opening; the surrounding colors indicate equivalent plastic strain (PEEQ) according to the legend and do not by themselves represent detached rock. Warmer colors indicate higher PEEQ values.

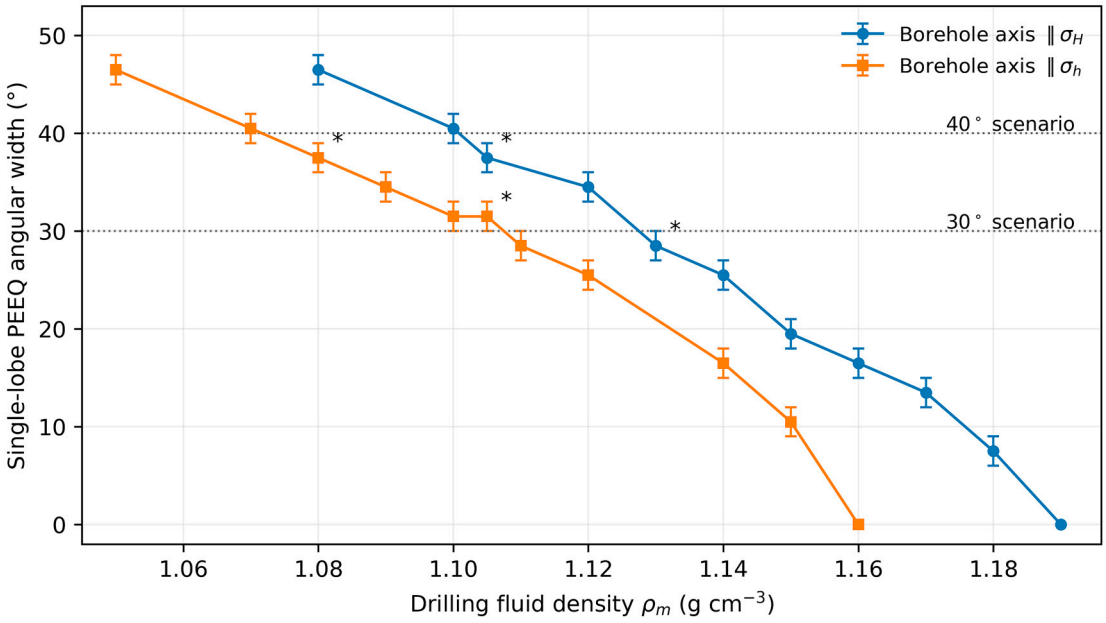


Figure 10. Variation in numerical potential collapse angular width with drilling fluid density for the two drilling orientations.

Table 5. Discretely identified single-lobe PEEQ angular widths for the 22 mud-weight cases under the two well orientations.

Drilling Parallel to σH		Drilling Parallel to σh	
Mud Weight (g/cm^3)	**Numerical Potential Collapse Width (°)**	**Mud Weight (g/cm^3)**	**Numerical Potential Collapse Width (°)**
1.08	45–48	1.05	45–48
1.10	39–42	1.07	39–42
1.12	33–36	1.09	33–36
1.14	24–27	1.10	30–33
1.15	18–21	1.11	27–30
1.16	15–18	1.12	24–27
1.17	12–15	1.14	15–18
1.18	6–9	1.15	9–12
1.19	0 (numerical zero)	1.16	0 (numerical zero)
1.105	36–39	1.080	36–39
1.130	27–30	1.105	30–33

4.6. Pore-Pressure Field Evolution and Its Influence on Moderate Collapse

To examine how drilling-fluid pressure affects near-wellbore effective stresses and plastic-zone development through seepage, pore-pressure fields were analyzed for different mud weights and well orientations. The Abaqus output variable POR denotes pore-fluid pressure within the porous formation. Initial and far-field pore pressures were both 41.78 MPa; prescribed wall pore pressure was set to the hydrostatic mud pressure for each case. Although POR is displayed in pascals in contour plots, values are reported in MPa in the text.

4.6.1. Pore-Pressure Distribution for Drilling Parallel to the Maximum Horizontal Principal Stress

Figure 11 shows POR distributions for a well parallel to σH at different mud weights. The prescribed wall pore pressure increases with the hydrostatic mud pressure, whereas far-field pore pressure remains as 41.78 MPa. Thus, increasing the mud weight from 1.08 to 1.19 g/cm^3 raises the wall pressure from approximately 44.06 to 48.55 MPa and establishes a transient gradient from the borehole toward the far field. A comparison with the PEEQ maps in Figure 8 shows that the numerical plastic angular extent decreases as the mud weight increases.

4.6.2. Pore-Pressure Distribution for Drilling Parallel to the Minimum Horizontal Principal Stress

Figure 12 shows POR fields at different mud weights for a well parallel to σh. Pore pressure likewise decreases from the borehole toward the far field. Increasing the mud weight from 1.05 to 1.16 g/cm^3 raises borehole pressure from 42.84 to 47.32 MPa, increasing both near-wall POR and the pressure difference between the borehole and far-field boundary. The contours remain approximately concentric at different mud weights. Under homogeneous isotropic hydraulic properties and identical pore-pressure boundary types, mud weight predominantly changes the magnitude of pore pressure rather than the general form of the diffusion field.

The pore-pressure fields for both orientations transition from the high prescribed borehole-wall pressure to the far-field initial pore pressure. In the ideal homogeneous model, cases with the same wall pore pressure and hydraulic parameters exhibit broadly similar pore-pressure patterns. However, the principal-stress arrangement in the bore-

hole cross-section produces different hoop effective-stress distributions and PEEQ angular domains.

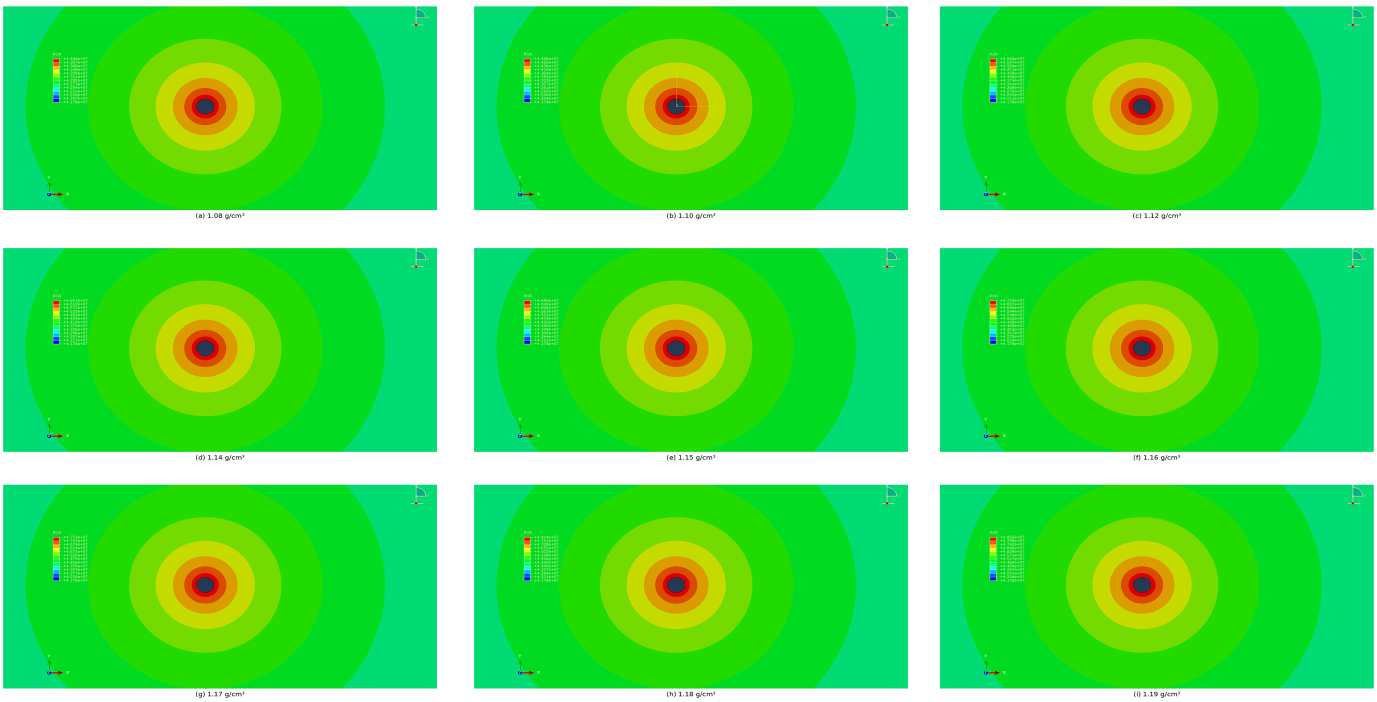


Figure 11. Pore-pressure (POR) distributions for drilling parallel to σH: (**a**) 1.08; (**b**) 1.10; (**c**) 1.12; (**d**) 1.14; (**e**) 1.15; (**f**) 1.16; (**g**) 1.17; (**h**) 1.18; and (**i**) 1.19 g/cm^3. The surrounding colors represent pore-pressure (POR) contours according to the legend; the central circular region denotes the borehole opening. The POR legend values are expressed in Pa.

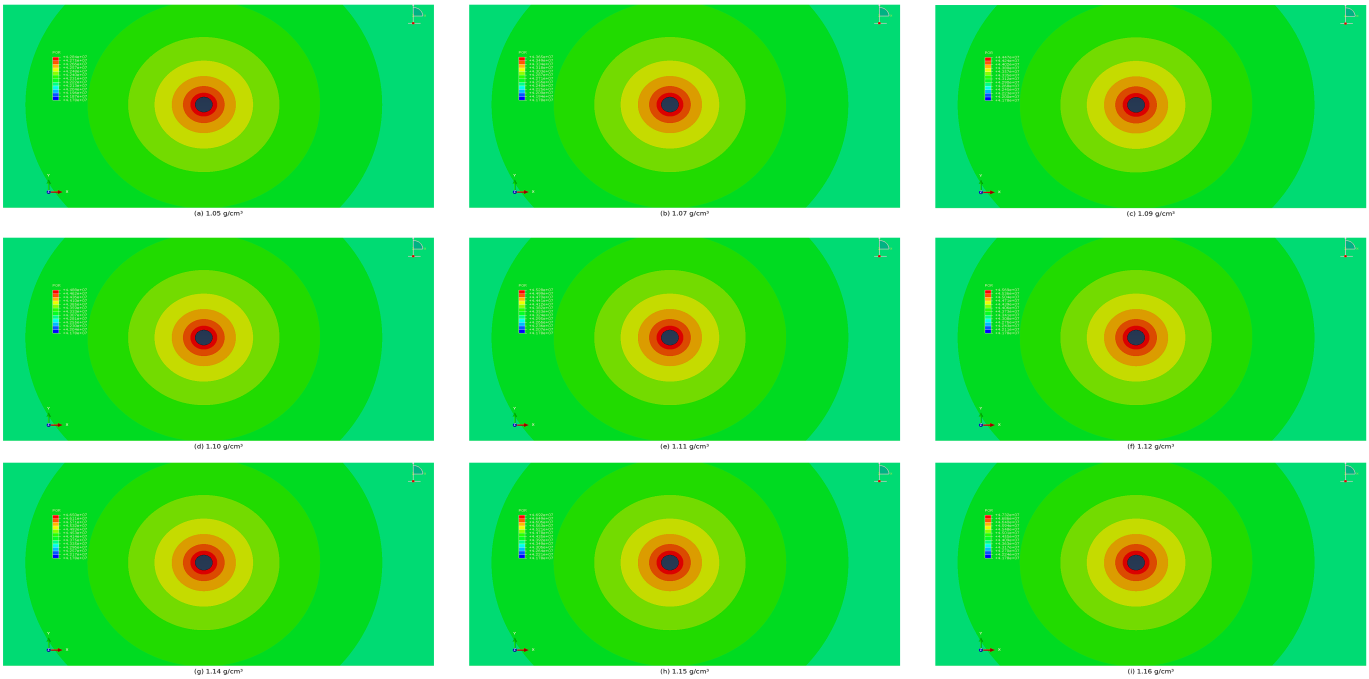


Figure 12. Pore-pressure (POR) distributions for drilling parallel to σh: (**a**) 1.05; (**b**) 1.07; (**c**) 1.09; (**d**) 1.10; (**e**) 1.11; (**f**) 1.12; (**g**) 1.14; (**h**) 1.15; and (**i**) 1.16 g/cm^3. The surrounding colors represent pore-pressure (POR) contours according to the legend; the central circular region denotes the borehole opening. The POR legend values are expressed in Pa.

4.7. Hoop Stress and Mechanisms of Plastic-Zone Development

4.7.1. Hoop-Stress Distribution for Drilling Parallel to the Maximum Horizontal Principal Stress

Figure 13 shows the hoop-stress distribution for a well parallel to σH. Compressive hoop stresses concentrate on opposite sides of the borehole, corresponding to the locations of potential PEEQ plastic lobes. Since both mechanical wall pressure and prescribed pore pressure rise with mud weight, near-wall effective stresses and plastic responses vary together. Under the idealized compression-positive boundary with $\alpha = 1$ and $p(R) = Pw$, the wall satisfies $\sigma r(R) = Pw$ and $\sigma' r(R) = \sigma r - p(R) = 0$. To quantify near-wellbore stress changes, radial, hoop, and axial effective stresses and pore pressure were extracted at $\theta = 180°$ and 90° for mud weights of 1.12 and 1.18 g/cm^3 in the σH-parallel orientation (Table 6).

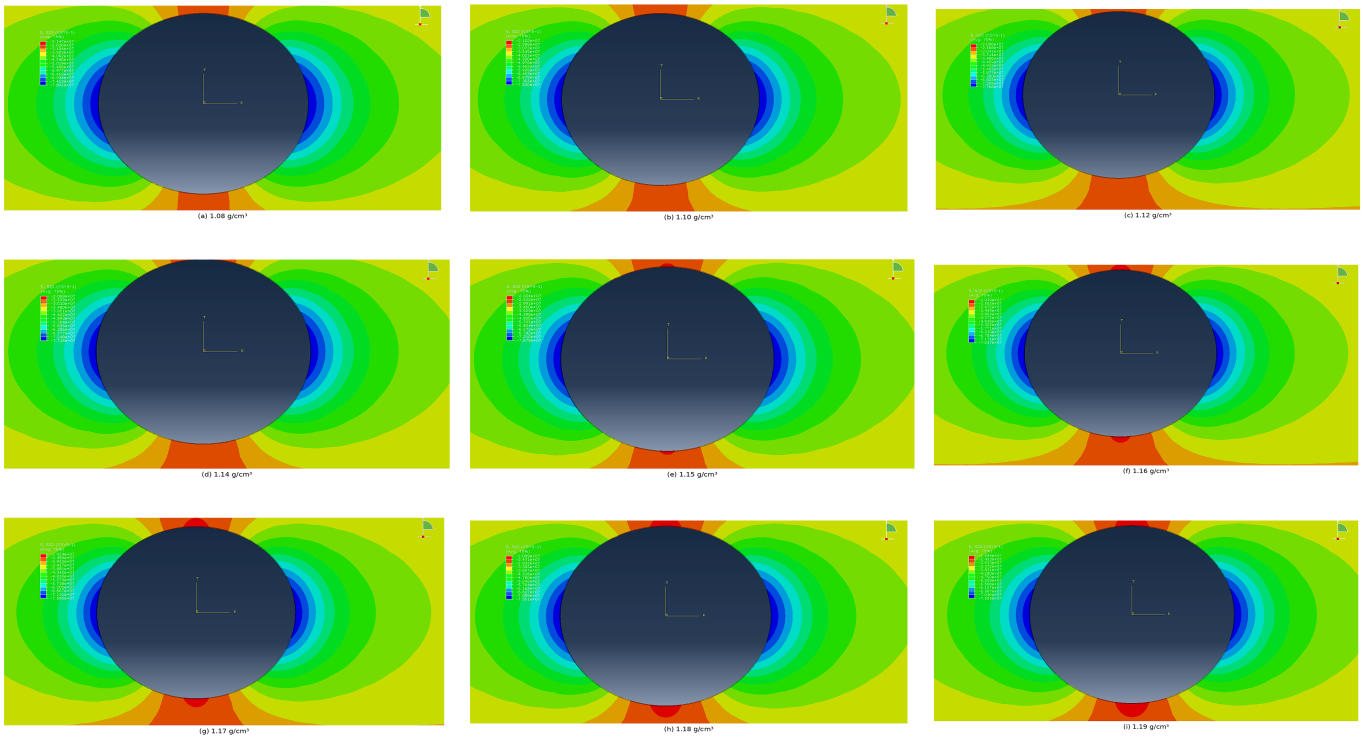


Figure 13. Hoop-stress distributions for drilling parallel to σH: (**a**) 1.08; (**b**) 1.10; (**c**) 1.12; (**d**) 1.14; (**e**) 1.15; (**f**) 1.16; (**g**) 1.17; (**h**) 1.18; and (**i**) 1.19 g/cm^3. The central dark circle depicts the borehole opening, and the surrounding color contours represent the hoop-stress distribution according to the color scale. The plotted Abaqus S22 values use the tension-positive convention (negative values indicate compression) and are displayed in Pa; the corresponding compressive stress magnitudes discussed in the text are reported as positive values in MPa.

Table 6. Effective stresses and pore pressure at representative circumferential locations under different drilling fluid densities.

θ (°)	ρ_m (g/cm^3)	σ'_r (MPa)	$\sigma'\theta$ (MPa)	$\sigma'z$ (MPa)	p (MPa)
180	1.12	3.746	77.681	29.017	45.692
180	1.18	2.678	75.509	29.198	48.140
90	1.12	2.922	26.317	21.642	45.692
90	1.18	2.811	23.540	21.077	48.140

As shown in Table 6, when the mud weight increases from 1.12 to 1.18 g/cm^3, the wall pore pressure increases from 45.692 to 48.140 MPa. The compressive hoop effective

stress decreases from 77.681 to 75.509 MPa at θ = 180° and from 26.317 to 23.540 MPa at θ = 90°. Radial effective stresses decrease slightly, whereas axial effective stresses vary less substantially. These results indicate weaker hoop compressive stress concentration at higher mud weight in the investigated cases and reflect the combined response to simultaneously increasing mechanical wall support and prescribed pore pressure.

4.7.2. Hoop-Stress Distribution for Drilling Parallel to the Minimum Horizontal Principal Stress

Figure 14 presents hoop-stress contours for representative mud weights in the σh-parallel orientation. Compressive hoop stresses again concentrate on opposite sides of the borehole; however, the concentrated region and PEEQ plastic zone are generally smaller than those for the σH-parallel orientation at equal or comparable mud weights. This is consistent with the smaller transverse principal-stress contrast in the σh-parallel model, indicating that well orientation governs the development and severity of compressive-shear plasticity by changing the stress configuration in the borehole cross-section.

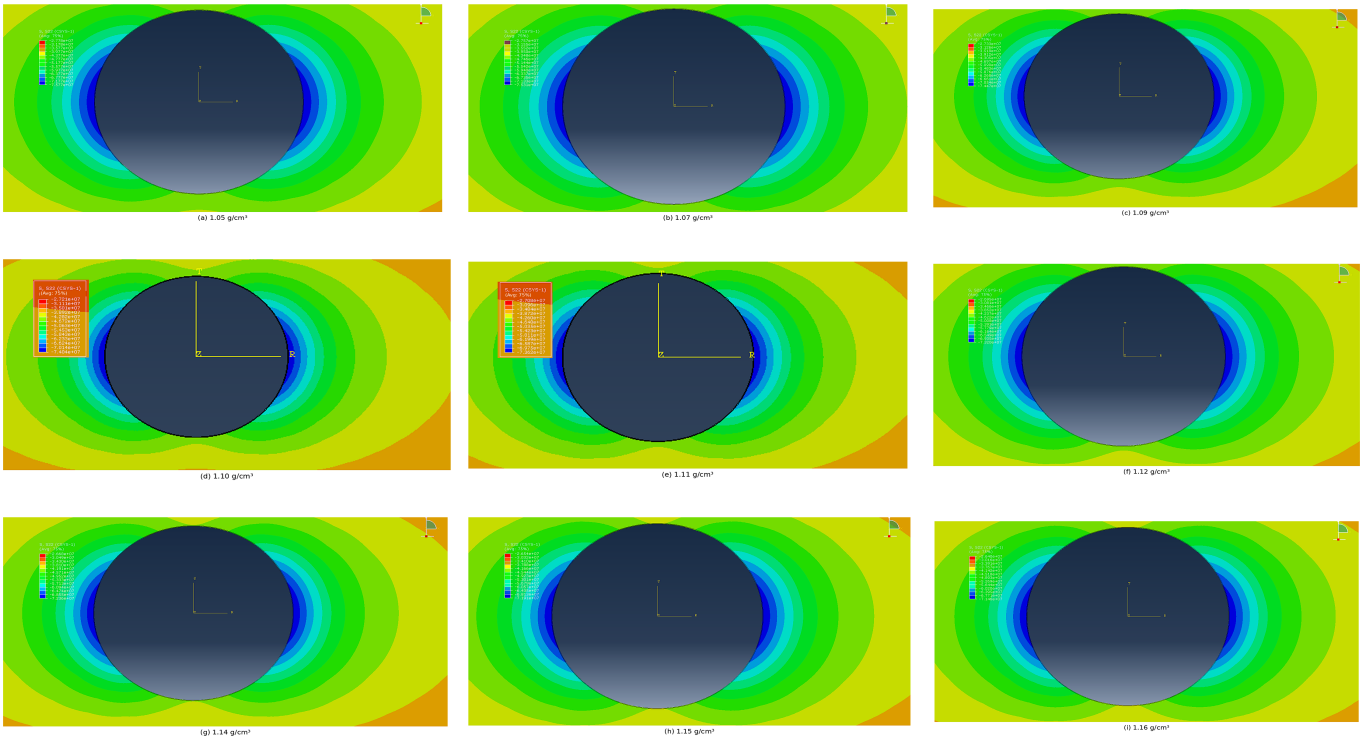


Figure 14. Hoop-stress distributions for drilling parallel to σh: (**a**) 1.05; (**b**) 1.07; (**c**) 1.09; (**d**) 1.10; (**e**) 1.11; (**f**) 1.12; (**g**) 1.14; (**h**) 1.15; and (**i**) 1.16 g/cm^3. The central dark circle depicts the borehole opening, and the surrounding color contours represent the hoop-stress distribution according to the color scale. The plotted Abaqus S22 values use the tension-positive convention (negative values indicate compression) and are displayed in Pa; the corresponding compressive stress magnitudes discussed in the text are reported as positive values in MPa.

4.7.3. Coupling Among Pore Pressure, Hoop Stress, and PEEQ Plastic Zones

For both well orientations, the POR field, hoop-stress contours, and PEEQ zones jointly describe the near-wellbore hydro-mechanical response to drilling-fluid pressure. POR displays an approximately axisymmetric decline from the wall toward the far field, whereas PEEQ lobes occur mainly on opposite sides of the borehole and coincide with zones of compressive hoop-stress concentration. This contrast indicates that pore pressure principally modulates skeleton stress through Biot's effective stress relationship rather than determining the circumferential location of plastic deformation by itself. The nonuniform in

situ stress configuration and associated hoop-stress concentration predominantly determine the azimuth and angular extent of potential collapse regions.

With increasing mud weight, radial support pressure and prescribed pore pressure increase simultaneously, resulting in coupled changes in pore-pressure and effective-stress fields. Under the investigated in situ stress, rock mechanical, and hydraulic properties, the compressive hoop effective stresses at representative circumferential locations decrease, as do the PEEQ plastic-zone extent and numerical potential collapse angular width β. These trends indicate suppression of overall compressive-shear plastic deformation at higher mud weight. They arise from the combined effects of mechanical wall support, pore-pressure diffusion, and effective-stress redistribution, which together govern stability under the specified boundary conditions.

4.8. Mud-Weight Optimization Based on Numerical Potential Collapse Angular Width

4.8.1. Mud-Weight Lower Bounds for Representative Sandstone

For the selected 30° and 40° numerical risk scenarios, the upper bound of each single-lobe angular-width interval, determined from the uniform PEEQ threshold and 1.5° circumferential sampling, was used as a conservative discrete screening criterion. A calculated mud-weight case was accepted if its angular-width upper bound did not exceed the prescribed limit. For a well parallel to σH, the angular widths at 1.105 and 1.130 g/cm^3 were 36–39° and 27–30°, respectively; for a well parallel to σh, they were 36–39° at 1.080 g/cm^3 and 27–30° at 1.110 g/cm^3. These are the evaluated mud weights meeting the 40° and 30° scenarios, respectively, among the discrete cases considered.

These mud weights are screening outcomes under the specified model, angular-width threshold, and risk scenario. Actual drilling-fluid design must also meet pore-pressure, lost-circulation, and fracture-pressure constraints and account for equivalent circulating density (ECD), surge pressures, hole cleaning, mud cake formation, filtrate invasion, and caliper response.

4.8.2. Lithology- and Orientation-Specific Engineering Recommendations

An integrated assessment of field pressure windows, inclination–azimuth trends, and representative-sandstone FEM results supports lithology- and orientation-specific mud-weight strategies. Mudstone intervals should not inherit mud-weight limits inferred from sandstone PEEQ angular domains; stability control should instead prioritize reduction of cavings and tight-hole problems. In representative sandstone, some local plasticity below the fully stable pressure may be permitted where hole cleaning and monitoring are adequate, preserving larger margins below the lost-circulation and fracture-pressure limits. A greater safety margin is appropriate when drilling parallel to σH or where caliper fluctuations and persistent cavings are evident. A relatively lower lower-bound mud weight may be considered in sandstone drilled parallel to σh when the borehole response remains stable.

Field mud weights, caliper data, and operational problems are used to assess the engineering plausibility of this strategy, not to establish that sandstone FEM thresholds directly apply to mudstone or the full well section. Field adjustments should be incremental and interval specific, accompanied by monitoring of returned cuttings, torque and drag, pump pressure, caliper response, and resistance during short trips. Persistent cavings, severe hole enlargement, deteriorating hole cleaning, or substantially increased tripping resistance should prompt timely mud-weight increases.

5. Discussion, Engineering Implications, and Applicability

5.1. Progressive Failure, Engineering Implications, and Economic Trade-Offs

A fully stable mud weight corresponds to the absence of yielding around the borehole circumference, whereas moderate-collapse design permits local plasticity provided its extent and subsequent development remain operationally manageable. Defining β from a continuous PEEQ angular domain converts the traditional binary question of whether the rock has yielded into a geometric risk indicator that changes with mud weight. Accordingly, β represents the potential failure extent, not the final geometry of detached rock.

From an engineering-economic perspective, excessive mud weight may suppress plastic yielding but reduce margins to lost-circulation and fracture pressures, increasing risks of remedial losses, downtime, and nonproductive time. Conversely, insufficient mud weight may increase cavings, hole enlargement, backreaming, tight-hole incidents, and hole-cleaning requirements. Moderate-collapse optimization therefore seeks a balance among wellbore instability risk, lost-circulation risk, and operational complexity rather than merely minimizing mud weight.

5.2. Field Consistency, Scope of Applicability, and Model Limitations

The two reference wells support two limited engineering observations. First, despite calculated collapse risks in some intervals, X1 exhibited an overall manageable final borehole diameter, and X2 pressure-window and operational records did not indicate persistently uncontrollable instability. This suggests a potential operational transition between initial yielding and unacceptable failure. Second, inclination–azimuth and lithological analyses demonstrate differences between sandstone and mudstone pressure windows, supporting lithology- and orientation-dependent mud-weight design.

The representative sandstone is modeled as a homogeneous isotropic saturated porous medium. Bedding-plane weakness, natural fractures, drilling-fluid chemistry, temperature changes, rock creep, post-peak softening, and removal of fragmented rock are not explicitly simulated. Pore–fracture connectivity can strongly affect fluid transport and pressure transmission [38]; hence, the homogeneous seepage assumption may inadequately characterize pore-pressure diffusion and potential failure extent in fractured or highly heterogeneous interbeds. Circulation-related temperature changes may also modify near-wellbore stability through thermal stresses [4], motivating future THM/THMC coupling. In addition, the fixed-mesh, small-deformation FEM cannot fully reproduce large-deformation spalling and post-collapse borehole geometry updates. Large-deformation, meshfree, and collocation-based methods offer potential avenues for future cross-validation [39]. Future work should calibrate the relationship between PEEQ angular domains and actual breakout using formation microimager (FMI), ultrasonic borehole imager (UBI), or multi-arm caliper data and assess uncertainty in stresses, strength, and pore pressure. Studies of heterogeneity and anisotropy [40–42] and of shale hydration, drilling-fluid/formation reactions, and time-dependent instability [43–45] further delineate phenomena excluded here; their quantitative findings are not transferred to the present sandstone model.

6. Conclusions

Using three-pressure profiles, actual drilling-fluid densities, and operational records from two vertical reference wells in a South China Sea deepwater gas field, conventional wellbore stability calculations were combined with Biot hydro-mechanically coupled–Mohr–Coulomb finite element simulations of representative sandstone. The effects of well orientation and mud weight on near-wellbore plastic responses and density-control strategies were investigated. The principal conclusions are as follows:

(1) In some sandstone–mudstone intervals of Wells X1 and X2, calculated collapse-pressure equivalent mud weights exceeded the actual drilling-fluid densities. The final borehole diameter in X1 remained broadly manageable after backreaming and other hole-conditioning operations. X2 provides pressure-window and operational evidence but lacks caliper records suitable for quantitative validation. These field observations suggest a potentially manageable range between theoretical incipient instability and operationally unacceptable wellbore damage; they do not establish actual breakout angular widths in horizontal wells.

(2) Conventional stability calculations give horizontal-well collapse-pressure equivalent mud weights of approximately 1.27–1.30 g/cm^3 for representative mudstone and 1.16–1.19 g/cm^3 for sandstone. Both lithology and drilling orientation affect the safe mud-weight window. Drilling parallel to the minimum horizontal principal stress σh gives a lower collapse-pressure bound and a higher fracture-pressure bound and is relatively favorable, whereas the opposite applies when drilling parallel to σH. These results characterize relative stability across lithologies and orientations, not the applicability of sandstone FEM predictions to mudstone.

(3) The full angular width β of a continuous PEEQ plastic lobe intersecting the borehole wall was used to evaluate the potential plastic extent in representative sandstone. Across 18 baseline and 4 locally refined cases, all evaluated at the 30-day transient endpoint with PEEQ > 10^{-8} and 1.5° angular sampling, β generally decreased as mud weight increased. At the same mud weight, drilling parallel to σh produced a narrower angular width than drilling parallel to σH. At 1.12 g/cm^3, the respective widths were 24–27° and 33–36°. No detectable wall-connected plastic lobe was observed at 1.16 g/cm^3 in the σh-parallel case or 1.19 g/cm^3 in the σH-parallel case.

(4) The 30° and 40° numerical risk-control scenarios, which have not been calibrated against field breakout widths, were applied using the upper bound of each angular-width interval for conservative screening. Among the calculated cases, mud weights of 1.105 and 1.130 g/cm^3 satisfy the 40° and 30° scenarios, respectively, for drilling parallel to σH; the corresponding values for drilling parallel to σh are 1.080 and 1.110 g/cm^3. These are discrete screening results conditioned on prescribed stresses, rock properties, hydraulic boundaries, and plastic-width identification rules, not field-validated critical mud weights for actual breakout. Operational application must also respect pore-pressure, lost-circulation, and fracture-pressure constraints.

(5) Pore pressure generally decreases from the borehole toward the far field, and PEEQ lobes form mainly in zones of compressive hoop-stress concentration. For drilling parallel to σH, increasing the mud weight from 1.12 to 1.18 g/cm^3 increased the prescribed wall pore pressure from 45.692 to 48.140 MPa. The compressive hoop effective stress decreased from 77.681 to 75.509 MPa at θ = 180° and from 26.317 to 23.540 MPa at θ = 90°, consistent with the reduction in plastic angular width. Because mechanical wall support and prescribed pore pressure were varied simultaneously, their separate contributions cannot be quantified from these results alone.

(6) The independent elastic Kirsch–FEM benchmark reproduced the principal locations and trends of near-wellbore stress concentration. Full-circumference RMSEs for radial, hoop, and axial stresses were 2.617, 2.425, and 2.054 MPa, respectively, providing a basic elastic benchmark for the numerical model. The PEEQ-based angular width represents potential plastic extent under a specified coupled loading history, not actual detached-rock geometry. Because mud cake sealing, thermo-chemical effects, fractures, post-peak softening, and block removal are not modeled, mud-weight optimization should account for lithology, orientation, hole cleaning, and real-time

monitoring. The relationship between numerical PEEQ width and field breakout width remains to be calibrated.

Author Contributions: Conceptualization, C.L.; Methodology, X.Z.; Software, H.F.; Validation, R.D.; Formal Analysis, H.S.; Investigation, Z.L.; Resources, A.Z.; Data Curation, C.Y. (Chen Yu); Writing—Original Draft, Y.H.; Writing—Review and Editing, X.L.; Visualization, C.Y. (Chuanliang Yan). All authors have read and agreed to the published version of the manuscript.

Funding: This research was funded by China National Offshore Oil Corporation (China), grant number KJZH-2025-2302.

Data Availability Statement: The original contributions presented in this study are included in the article. Further inquiries can be directed to the corresponding author.

Conflicts of Interest: Author Chenglong Li, Xuanhua Zhu, Rui Dai, Haolin Song, Zheng Liu, Aopeng Zhang, Chen Yu, Yulong He, and Xin Li were employed by CNOOC China Limited. The remaining authors declare that the research was conducted in the absence of any commercial or financial relationships that could be construed as a potential conflict of interest. The authors declare that this study received funding from China National Offshore Oil Corporation. The funder was not involved in the study design; collection, analysis, or interpretation of data; the writing of this article; or the decision to submit it for publication.

References

1. Fjær, E.; Holt, R.M.; Horsrud, P.; Raaen, A.M.; Risnes, R. *Petroleum Related Rock Mechanics*, 2nd ed.; Elsevier: Amsterdam, The Netherlands, 2008.
2. Zoback, M.D. *Reservoir Geomechanics*; Cambridge University Press: Cambridge, UK, 2007.
3. Aadnoy, B.S.; Looyeh, R. *Petroleum Rock Mechanics: Drilling Operations and Well Design*; Gulf Professional Publishing: Oxford, UK, 2011.
4. Wang, Q.; Xu, Z.; Jia, W.; Song, X.; Li, G.; Zhou, M.; Qu, H.; Huang, S.; Gou, T.; Yuan, Z. Active wellbore cooling during deep drilling circulation via microencapsulated phase change materials: Energy redistribution mechanism and inverse design. *Energy* **2026**, *360*, 141647. [CrossRef]
5. Bradley, W.B. Failure of inclined boreholes. *J. Energy Resour. Technol.* **1979**, *101*, 232–239. [CrossRef]
6. Aadnoy, B.S.; Chenevert, M.E. Stability of highly inclined boreholes. *SPE Drill. Eng.* **1987**, *2*, 364–374. [CrossRef]
7. Zoback, M.D.; Moos, D.; Mastin, L.; Anderson, R.N. Well bore breakouts and in situ stress. *J. Geophys. Res.* **1985**, *90*, 5523–5530. [CrossRef]
8. Mastin, L. Effect of borehole deviation on breakout orientations. *J. Geophys. Res. Solid Earth* **1988**, *93*, 9187–9195. [CrossRef]
9. Peška, P.; Zoback, M.D. Compressive and tensile failure of inclined well bores and determination of in situ stress and rock strength. *J. Geophys. Res. Solid Earth* **1995**, *100*, 12791–12811. [CrossRef]
10. Haimson, B.C.; Song, I. Laboratory study of borehole breakouts in Cordova Cream: A case of shear failure mechanism. *Int. J. Rock Mech. Min. Sci. Geomech. Abstr.* **1993**, *30*, 1047–1056. [CrossRef]
11. Lee, M.Y.; Haimson, B.C. Laboratory study of borehole breakouts in Lac du Bonnet granite: A case of extensile failure mechanism. *Int. J. Rock Mech. Min. Sci. Geomech. Abstr.* **1993**, *30*, 1039–1045. [CrossRef]
12. Haimson, B.C. Micromechanisms of borehole instability leading to breakouts in rocks. *Int. J. Rock Mech. Min. Sci.* **2007**, *44*, 157–173. [CrossRef]
13. Liu, H.; Gao, X.; Yan, B.; Wang, S.; Zhou, Z.; Jiang, X. Reconstruction of Block Model of Tunnel Surrounding Rock and Prediction Method of Chain Collapse Process. *Rock Mech. Rock Eng.* **2026**, *59*, 7669–7689. [CrossRef]
14. Zheng, Y.; Li, J.; Zhu, T.; Zhang, L. Cascading failure in levee systems: A two-stage material point method framework. *Comput. Geotech.* **2026**, *194*, 108039. [CrossRef]
15. Moos, D.; Peška, P.; Finkbeiner, T.; Zoback, M. Comprehensive wellbore stability analysis utilizing quantitative risk assessment. *J. Pet. Sci. Eng.* **2003**, *38*, 97–109. [CrossRef]
16. Moos, D. Wellbore Stability in Deep Water—Handling Geomechanical Uncertainty. In *Proceedings of the AADE 2001 National Drilling Conference, Houston, TX, USA, 27–29 March 2001*; AADE 01-NC-HO-43; American Association of Drilling Engineers: Houston, TX, USA, 2001.
17. Mody, F.K.; Hale, A.H. Borehole-stability model to couple the mechanics and chemistry of drilling-fluid/shale interactions. *J. Pet. Technol.* **1993**, *45*, 1093–1101. [CrossRef]

18. Hale, A.H.; Mody, F.K.; Salisbury, D.P. The influence of chemical potential on wellbore stability. *SPE Drill. Complet.* **1993**, *8*, 207–216. [CrossRef]
19. van Oort, E.; Hale, A.H.; Mody, F.K.; Roy, S. Transport in shales and the design of improved water-based shale drilling fluids. *SPE Drill. Complet.* **1996**, *11*, 137–146. [CrossRef]
20. van Oort, E. On the physical and chemical stability of shales. *J. Pet. Sci. Eng.* **2003**, *38*, 213–235. [CrossRef]
21. Chen, G.; Chenevert, M.E.; Sharma, M.M.; Yu, M. A study of wellbore stability in shales including poroelastic, chemical, and thermal effects. *J. Pet. Sci. Eng.* **2003**, *38*, 167–176. [CrossRef]
22. Ghassemi, A.; Diek, A. Porothermoelasticity for swelling shales. *J. Pet. Sci. Eng.* **2002**, *34*, 123–135. [CrossRef]
23. Yu, M.; Chenevert, M.E.; Sharma, M.M. Chemical-mechanical wellbore instability model for shales: Accounting for solute diffusion. *J. Pet. Sci. Eng.* **2003**, *38*, 131–143. [CrossRef]
24. Biot, M.A. General theory of three-dimensional consolidation. *J. Appl. Phys.* **1941**, *12*, 155–164. [CrossRef]
25. Rice, J.R.; Cleary, M.P. Some basic stress diffusion solutions for fluid-saturated elastic porous media with compressible constituents. *Rev. Geophys.* **1976**, *14*, 227–241. [CrossRef]
26. Detournay, E.; Cheng, A.H.-D. Poroelastic response of a borehole in a non-hydrostatic stress field. *Int. J. Rock Mech. Min. Sci. Geomech. Abstr.* **1988**, *25*, 171–182. [CrossRef]
27. Wang, H.F. *Theory of Linear Poroelasticity with Applications to Geomechanics and Hydrogeology*; Princeton University Press: Princeton, NJ, USA, 2000.
28. Ewy, R.T. Wellbore-stability predictions by use of a modified Lade criterion. *SPE Drill. Complet.* **1999**, *14*, 85–91. [CrossRef]
29. Al-Ajmi, A.M.; Zimmerman, R.W. Relation between the Mogi and the Coulomb failure criteria. *Int. J. Rock Mech. Min. Sci.* **2005**, *42*, 431–439. [CrossRef]
30. Al-Ajmi, A.M.; Zimmerman, R.W. Stability analysis of vertical boreholes using the Mogi-Coulomb failure criterion. *Int. J. Rock Mech. Min. Sci.* **2006**, *43*, 1200–1211. [CrossRef]
31. Benz, T.; Schwab, R. A quantitative comparison of six rock failure criteria. *Int. J. Rock Mech. Min. Sci.* **2008**, *45*, 1176–1186. [CrossRef]
32. Gholami, R.; Moradzadeh, A.; Rasouli, V.; Hanachi, J. Practical application of failure criteria in determining safe mud weight windows in drilling operations. *J. Rock Mech. Geotech. Eng.* **2014**, *6*, 13–25. [CrossRef]
33. Manshad, A.K.; Jalalifar, H.; Aslannejad, M. Analysis of vertical, horizontal and deviated wellbores stability by analytical and numerical methods. *J. Pet. Explor. Prod. Technol.* **2014**, *4*, 359–369. [CrossRef]
34. Papanastasiou, P.; Zervos, A. Wellbore stability analysis: From linear elasticity to postbifurcation modelling. *Int. J. Geomech.* **2004**, *4*, 2–12. [CrossRef]
35. Li, X.; El Mohtar, C.S.; Gray, K.E. 3D poro-elasto-plastic modeling of breakouts in deviated wells. *J. Pet. Sci. Eng.* **2019**, *174*, 913–920. [CrossRef]
36. Sahara, D.P.; Schoenball, M.; Gerolymatou, E.; Kohl, T. Analysis of borehole breakout development using continuum damage mechanics. *Int. J. Rock Mech. Min. Sci.* **2017**, *97*, 134–143. [CrossRef]
37. Lin, H.; Kang, W.H.; Oh, J.; Canbulat, I.; Hebblewhite, B. Numerical simulation on borehole breakout and borehole size effect using discrete element method. *Int. J. Min. Sci. Technol.* **2020**, *30*, 623–633. [CrossRef]
38. Sun, M.; Duan, X.; Liu, Q.; Blach, T.P.; Ostadhassan, M.; Liu, B.; Ji, Y.; Hu, Q.; Pan, Z. The importance of pore-fracture connectivity in overmature marine shale for methane occurrence and transportation. *Mar. Pet. Geol.* **2023**, *157*, 106495. [CrossRef]
39. Hong, A.; Liao, X.; Zheng, H.; Zhuang, X. Simulation of soil collapse based on the local radial basis function collocation method. *Eng. Anal. Bound. Elem.* **2026**, *186*, 106687. [CrossRef]
40. Kanfar, M.F.; Chen, Z.; Rahman, S.S. Risk-controlled wellbore stability analysis in anisotropic formations. *J. Pet. Sci. Eng.* **2015**, *134*, 214–222. [CrossRef]
41. Ong, S.H.; Roegiers, J.-C. Influence of anisotropies in borehole stability. *Int. J. Rock Mech. Min. Sci. Geomech. Abstr.* **1993**, *30*, 1069–1075. [CrossRef]
42. Gough, D.I.; Bell, J.S. Stress orientations from borehole wall fractures with examples from Colorado, east Texas, and northern Canada. *Can. J. Earth Sci.* **1982**, *19*, 1358–1370. [CrossRef]
43. Bol, G.M.; Wong, S.-W.; Davidson, C.J.; Woodland, D.C. Borehole stability in shales. *SPE Drill. Complet.* **1994**, *9*, 87–94. [CrossRef]
44. Chenevert, M.E. Shale alteration by water adsorption. *J. Pet. Technol.* **1970**, *22*, 1141–1148. [CrossRef]
45. Yan, C.-L.; Dong, L.-F.; Zhao, K.; Cheng, Y.-F.; Li, X.-R.; Deng, J.-G.; Li, Z.-Q.; Chen, Y. Time-dependent borehole stability in hard-brittle shale. *Pet. Sci.* **2022**, *19*, 663–677. [CrossRef]

Disclaimer/Publisher's Note: The statements, opinions and data contained in all publications are solely those of the individual author(s) and contributor(s) and not of MDPI and/or the editor(s). MDPI and/or the editor(s) disclaim responsibility for any injury to people or property resulting from any ideas, methods, instructions or products referred to in the content.